

**REVERSIBLE HYDROGEN STORAGE OF  
NANOCONFINED  $\text{LiBH}_4$  IN POLY (METHYL  
METHACRYLATE)-co-BUTYL METHACRYLATE  
POLYMER MATRIX**



**Sukanya Meethom**

**A Thesis Submitted in Partial Fulfillment of the Requirements for the**

**Degree of Master of Science in Biochemistry**

**Suranaree University of Technology**

**Academic Year 2013**

กระบวนการกักเก็บไฮโดรเจนที่ผันกลับได้ของลิเทียมโพรไฮไดรด์ที่บรรจุ  
ระดับนาโนในเมทริกซ์โพลีเมอร์ของโพลีเมทิลเมทาคริเลต-โค-บิวทิล  
เมทาคริเลต



นางสาวสุกัญญา มีถม

วิทยานิพนธ์นี้เป็นส่วนหนึ่งของการศึกษาตามหลักสูตรปริญญาวิทยาศาสตรมหาบัณฑิต  
สาขาวิชาชีวเคมี  
มหาวิทยาลัยเทคโนโลยีสุรนารี  
ปีการศึกษา 2556

**REVERSIBLE HYDROGEN STORAGE OF NANOCONFINED  
LiBH<sub>4</sub> IN POLY (METHYL METHACRYLATE)-co-BUTYL  
METHACRYLATE POLYMER MATRIX**

Suranaree University of Technology has approved this thesis submitted in partial fulfillment of the requirements for a Master's Degree.

Thesis Examining Committee

---

(Assoc. Prof. Dr. Jatuporn Wittayakun)

Chairperson

---

(Asst. Prof. Dr. Rapee Gosalawit)

Member (Thesis Advisor)

---

(Assoc. Prof. Dr. Jaruwan Siritapetawee)

Member

---

(Asst. Prof. Dr. Sanchai Prayoonpokarach)

Member

---

(Dr. Theeranun Siritanon)

Member

---

(Prof. Dr. Sukit Limpijumnong)

Vice Rector for Academic Affairs  
and Innovation

---

(Assoc. Prof. Dr. Prapun Manyum)

Dean of Institute of Science

สุกัญญา มีถม : กระบวนการกักเก็บไฮโดรเจนที่ผันกลับได้ของลิเทียมโพรไซโคโรดที่  
บรรจุระดับนาโนในเมทริกซ์โพลีเมอร์ของโพลีเมทิลเมทาคริเลต-โค-บิวทิลเมทาคริ  
เลต (REVERSIBLE HYDROGEN STORAGE OF NANOCONFINED LiBH<sub>4</sub> IN POLY  
(METHYL METHACRYLATE)-co-BUTYL METHACRYLATE POLYMER  
MATRIX) อาจารย์ที่ปรึกษา : ผู้ช่วยศาสตราจารย์ ดร.ระพี โกศลวิตร, 77 หน้า.

การบรรจุในระดับนาโนเมตรของลิเทียมโพรไซโคโรดในโพลีเมทิลเมทาคริเลต-โค-  
บิวทิลเมทาคริเลตถูกคาดหวังให้เป็นระบบกักเก็บไฮโดรเจนที่ผันกลับได้ เนื่องจากคุณสมบัติการ  
ไม่ชอบน้ำและมีปริมาตรที่ว่างในเมทริกซ์โพลีเมอร์สูงสำหรับการแพร่ผ่านของไฮโดรเจนของโพลี  
เมทิลเมทาคริเลต-โค-บิวทิลเมทาคริเลต จึงสามารถหลีกเลี่ยงการเกิดปฏิกิริยาของลิเทียมโพร  
ไซโคโรดกับอากาศได้หลังจากการบรรจุเข้าไปในโพลีเมทิลเมทาคริเลต-โค-บิวทิลเมทาคริเลต  
อุณหภูมิเริ่มต้นที่ใช้ในการเกิดปฏิกิริยาการปล่อยไฮโดรเจนลดลงมาที่ 80 °C ( $\Delta T=210$  และ 170 °C  
เมื่อเปรียบเทียบกับลิเทียมโพรไซโคโรดที่มีขนาดในระดับนาโนเมตร และ ลิเทียมโพรไซโคโรดที่  
บรรจุในคาร์บอนแอโรเจล ตามลำดับ) นอกจากนี้ยังพบว่าจลนพลศาสตร์ของการปล่อยไฮโดรเจน  
ของระบบที่มีการบรรจุในระดับนาโนเมตรของลิเทียมโพรไซโคโรดเข้าไปในโพลีเมทิลเมทาคริ  
เลต-โค-บิวทิลเมทาคริเลตนี้เกิดได้เร็วขึ้นอย่างมีนัยสำคัญ เช่น การเกิดปฏิกิริยาการปล่อย  
ไฮโดรเจนในรอบแรกเกิดที่ 120 °C ในระบบสุญญากาศ และให้ไฮโดรเจนออกมา 5.96 wt. % เมื่อ  
เทียบกับปริมาณของลิเทียมโพรไซโคโรด ภายในเวลา 2 ชั่วโมง 30 นาที ในขณะที่ลิเทียมโพรไซ  
โคโรดที่มีขนาดในระดับนาโนเมตรไม่มีการปล่อยไฮโดรเจนออกมาที่อุณหภูมิเดียวกัน นอกจากนั้น  
ยังสามารถบอกได้ว่า ลิเทียมโพรไซโคโรดที่บรรจุเข้าไปในโพลีเมทิลเมทาคริเลต-โค-บิวทิล  
เมทาคริเลต สามารถเกิดปฏิกิริยาผันกลับเพื่อดูดไฮโดรเจนกลับคืนมาได้ที่สภาวะอ่อนที่สุด (140  
°C ภายใต้ความดันไฮโดรเจนที่ 50 บาร์และใช้เวลา 12 ชั่วโมงในการทำปฏิกิริยา) ซึ่งต่ำกว่าการ  
พัฒนาของลิเทียมโพรไซโคโรดด้วยวิธีอื่นๆที่เคยทำมา ในระบบนี้ปฏิสัมพันธ์ระหว่างลิเทียมโพร  
ไซโคโรดที่อะตอมของโบรอนกับโพลีเมทิลเมทาคริเลต-โค-บิวทิลเมทาคริเลตที่หมู่เอสเทอร์  
ซึ่งทำให้เกิดปฏิกิริยาผันกลับไม่สมบูรณ์ควรหลีกเลี่ยงในการพัฒนาระบบนี้ในอนาคต

สาขาวิชาชีวเคมี  
ปีการศึกษา 2556

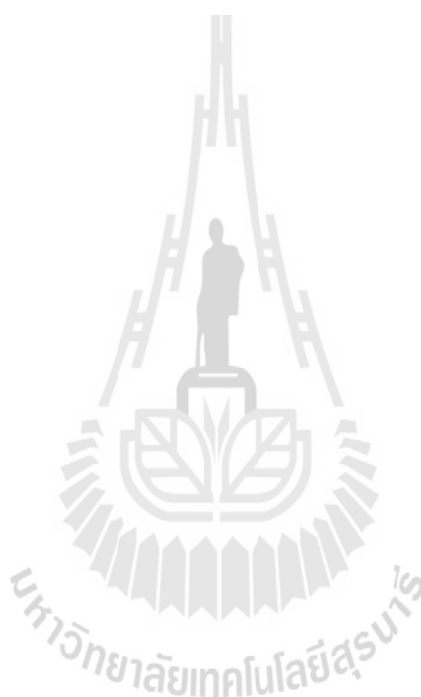
ลายมือชื่อนักศึกษา \_\_\_\_\_  
ลายมือชื่ออาจารย์ที่ปรึกษา \_\_\_\_\_

SUKANYA MEETHOM : REVERSIBLE HYDROGEN STORAGE OF  
NANOCONFINED  $\text{LiBH}_4$  IN POLY (METHYL METHACRYLATE)-co-BUTYL  
METHACRYLATE POLYMER MATRIX. THESIS ADVISOR : ASST. PROF.  
RAPEE GOSALAWIT, Ph.D. 77 PP.

HYDROGEN STORAGE/NANOCONFINEMENT/PMMA/  
LITHIUMBOROHYDRY/POLYMER

Nanoconfinement of  $\text{LiBH}_4$  in poly (methyl methacrylate)-co-butyl methacrylate (PMMA-co-BM), denoted as nanoconfined  $\text{LiBH}_4$ -PMMA-co-BM, is proposed for reversible hydrogen storage. Due to the hydrophobic property and higher free volume in the polymer matrix for  $\text{H}_2$  permeability of PMMA-co-BM, deterioration of  $\text{LiBH}_4$  by oxygen and humidity in ambient conditions is avoided after nanoconfinement in PMMA-co-BM. The onset dehydrogenation temperature nanoconfined  $\text{LiBH}_4$ -PMMA-co-BM is reduced to  $\sim 80$  °C ( $\Delta T=210$  and  $170$  °C compared with milled  $\text{LiBH}_4$  and nanoconfined  $\text{LiBH}_4$  in carbon aerogel, respectively). Moreover, significantly faster dehydrogenation kinetics are observed by using PMMA-co-BM as a host for  $\text{LiBH}_4$  nanoconfinement, for example, nanoconfined  $\text{LiBH}_4$ -PMMA-co-BM requires only 2 h 30 min ( $T=120$  °C under vacuum) to release 5.96 wt.%  $\text{H}_2$  with respect to  $\text{LiBH}_4$  content, while milled  $\text{LiBH}_4$  releases no hydrogen at the same temperature and pressure condition. Besides, it should be remarked that nanoconfined  $\text{LiBH}_4$ -PMMA-co-BM can be rehydrogenated at the mildest condition ( $140$  °C under 50 bar  $\text{H}_2$  for 12 h) among those reported for modified  $\text{LiBH}_4$  in the previous literatures. Interaction between

LiBH<sub>4</sub> and the ester group of PMMA-co-BM yields incomplete reversibility of the system, and should be avoided in the future development of this system.



School of Biochemistry

Academic Year 2013

Student's Signature\_\_\_\_\_

Advisor's Signature\_\_\_\_\_

## **ACKNOWLEDGEMENTS**

I would like to thank everyone who has helped me throughout my studies. First of all, I would like to thank my advisor, Asst. Prof. Dr. Rapee Gosalawit, for sharing her knowledge with me and editing my thesis. I am also thankful to the thesis examining committee, including Assoc. Prof. Dr. Jatuporn Wittayakun, Assoc. Prof. Dr. Jaruwan Siritapetawee, Asst. Prof. Dr. Sanchai Prayoonpokarach, and Dr. Theeranun Siritanon for their help and suggestions during my thesis defense.

I would like to acknowledge the Suranaree University of Technology for financial support. I would like to thank Dr. Hideki Nakajima (beamline 3.2a: PES, Synchrotron Light Research Institute, Thailand) and Dr. Yanling Hua (The Center for Scientific and Technological Equipment, Suranaree University of Technology, Thailand) for technical help and suggestions during XPS and solid NMR measurements, respectively.

Sukanya Meethom

# CONTENTS

	<b>Page</b>
ABSTRACT IN THAI.....	I
ABSTRACT IN ENGLISH .....	II
ACKNOWLEDGEMENTS.....	IV
CONTENTS.....	V
LIST OF TABLES .....	VIII
LIST OF FIGURES .....	IX
<b>CHAPTER</b>	
<b>I INTRODUCTION.....</b>	<b>1</b>
1.1 Hydrogen Energy.....	1
1.2 Fuel Cells .....	6
1.3 References.....	13
<b>II LITERATURE REVIEW.....</b>	<b>15</b>
2.1 Catalytic Modifications.....	16
2.2 Reactive Hydride Composites (RHCs) .....	19
2.3 Nanoconfinement in Nanoporous Scaffolds .....	23
2.4 Metal Hydride Polymer Composites.....	28
2.5 Research Objectives .....	35
2.6 References .....	35
<b>III EXPERIMENT.....</b>	<b>40</b>



## CONTENTS (Continued)

	<b>Page</b>
3.1 Sample Preparation .....	40
3.1.1 Purification of tetrahydrofuran .....	40
3.1.2 Precipitation of poly (methyl methacrylate )-co-butyl methacrylate .....	40
3.1.3 Synthesis of nanoconfined LiBH <sub>4</sub> in poly (methyl methacrylate) -co-butyl methacrylate (PMMA-co-BM).....	40
3.1.4 Preparation of milled LiBH <sub>4</sub> .....	41
3.2 Characterizations.....	41
3.2.1 Powder X-ray diffraction (XRD) measurement .....	41
3.2.2 Scanning electron microscopy (SEM) .....	42
3.2.3 Coupled manometric-calorimetric measurement.....	42
3.2.4 Gas analysis .....	42
3.2.5 Kinetic measurement.....	43
3.2.6 Fourier transform infrared spectroscopy (FTIR) .....	44
3.2.7 Nuclear magnetic resonance (NMR) measurement.....	45
3.2.8 X-ray photoelectron spectroscopy (XPS).....	45
3.3 References .....	46
<b>IV RESULT AND DISCUSSION.....</b>	<b>47</b>
4.1 Results and Discussion.....	47

## CONTENTS (Continued)

	<b>Page</b>
4.1.1 Nanoconfinement of LiBH <sub>4</sub> in PMMA-co-BM polymer matrix .....	47
4.1.2 Dehydrogenation profiles .....	50
4.1.3 Dehydrogenation kinetics and reversibility.....	54
4.1.4 Interaction between LiBH <sub>4</sub> and PMMA-co-BM.....	56
4.1.5 Protection from oxidation and humidity .....	63
4.1.6 Reaction mechanisms and reversibility.....	65
4.2 References .....	68
<b>V CONCLUSION</b> .....	71
<b>APPENDICES</b> .....	73
<b>APPENDIX A</b> <b>CALCULATION OF HYDROGEN CAPACITY</b> .....	74
<b>APPENDIX B</b> <b>THESIS OUTPUT</b> .....	76
<b>CURRICULUM VITAE</b> .....	77

## LIST OF TABLES

Table	Page
1.1 Comparison of fuel cell types .....	6
1.2 Comparison of three major competing technologies for hydrogen storage .....	10
1.3 US DOE Freedom CAR hydrogen storage system targets .....	12
4.1 Amount of components and theoretical and experimental hydrogen storage capacities of milled and nanoconfined samples .....	50

## LIST OF FIGURES

Figure	Page
1.1 Hydrogen sources.....	2
1.2 Hydrogen processing .....	3
1.3 Bio-hydrogen processing cycle.....	4
1.4 Components of fuel cell vehicles (FCVs).....	5
1.5 Polymer electrolyte membrane fuel cells (PEMFCs) .....	7
1.6 Reaction mechanisms in PEMFC .....	8
1.7 Hydrogen storage tanks of (A) compress hydrogen gas tank, (B) liquid hydrogen tank, and (C) solid state tank.....	11
2.1 Dehydrogenation (DH)/rehydrogenation (RH) profiles between (a) $\text{LiBH}_4+1/2\text{Al}+0.04\text{TiF}_3$ and (b) $\text{LiBH}_4+0.04\text{TiF}_3$ .....	17
2.2 TGA and RGA spectra of the material $\text{LiBH}_4+0.2\text{MgCl}_2+0.1\text{TiCl}_3$ .....	18
2.3 Isothermal rehydrogenation of the material $\text{LiBH}_4+0.2\text{MgCl}_2+$ $0.1\text{TiCl}_3$ .....	19
2.4 Absorption/desorption isotherms at 315-450 °C for the $\text{LiBH}_4 + 1/2\text{MgH}_2$ system.....	20
2.5 Van't Hoff plots of destabilized (a) $\text{LiBH}_4+1/2\text{MgH}_2$ , (b) pure $\text{LiBH}_4$ , and (c) $\text{MgH}_2$ .....	21
2.6 In situ XRD measurement of the desorption reaction of $2\text{LiBH}_4-$ $\text{MgH}_2$ composite doped with 5 wt. % titanium isopropoxide .....	22

## LIST OF FIGURES (Continued)

Figure	Page
2.7	B <sub>2</sub> H <sub>6</sub> and H <sub>2</sub> release with increasing temperature for LiBH <sub>4</sub> @ nanoporous carbon (NPC) 4 nm, LiBH <sub>4</sub> @ carbon aerogel (CA) 9 nm, and LiBH <sub>4</sub> @CA-15 nm. The loading of each sample is 10 wt. % ..... 25
2.8	Normalized hydrogen desorption profiles of the nanoconfined 2LiBH <sub>4</sub> -MgH <sub>2</sub> and bulk 2LiBH <sub>4</sub> -MgH <sub>2</sub> ..... 27
2.9	SEM images of standard polyaniline before ((a) and (b)) and after hydrogen sorption ((c) and (d))..... 29
2.10	Hydrogen sorption measurements of polyaniline (A) and polyaniline with 30 wt.% aluminum powder (B) at different temperatures and increasing pressure ..... 30
2.11	Hydrogen (a) adsorption and (b) desorption PCT curves for the polyaniline fibers ..... 31
2.12	SEM micrographs of polyaniline fibers (a) before and (b) after hydrogen sorption cycles ..... 32
2.13	SEM micrographs of as prepared PS-LaNi <sub>5</sub> (A) and PVP-Pd (B) composites..... 33
2.14	Mg NCs in a gas-barrier polymer matrix ..... 34
2.15	Chemical structures of PMMA (A) and PMMA-co-BM (B) ..... 35
3.1	Schematic diagram of Sievert-type apparatus ..... 44
4.1	XRD patterns of PMMA-co-BM (a) and nanoconfined

## LIST OF FIGURES (Continued)

Figure	Page
LiBH <sub>4</sub> -PMMA-co-BM (b) .....	48
4.2 SEM image of nanoconfined LiBH <sub>4</sub> -PMMA PMMA-co-BM (A), carbon mapping (B), oxygen mapping (C), boron mapping (D), and quantitative elemental analysis (E) .....	49
4.3 Dehydrogenation profiles and hydrogen storage capacities from coupled manometric-calorimetric analysis of milled LiBH <sub>4</sub> .....	51
4.4 Dehydrogenation profiles from coupled manometric-calorimetric analysis of nanoconfined LiBH <sub>4</sub> -PMMA-co-BM .....	52
4.5 Gas analyses during desorption of nanoconfined LiBH <sub>4</sub> -PMMA-co-BM .....	53
4.6 Dehydrogenation kinetics of nanoconfined LiBH <sub>4</sub> -PMMA-co-BM, milled LiBH <sub>4</sub> , and PMMA-co-BM at 120 °C .....	55
4.7 FTIR spectra of LiBH <sub>4</sub> (a), PMMA-co-BM (b), and nanoconfined LiBH <sub>4</sub> -PMMA-co-BM (c) .....	58
4.8 Chemical structure (A) and <sup>13</sup> C NMR (B) of PMMA-co-BM .....	59
4.9 Chemical structure (A) and <sup>13</sup> C NMR (B) of nanoconfined LiBH <sub>4</sub> -PMMA-co-BM (B) .....	60
4.10 Interaction between PMMA-co-BM and LiBH <sub>4</sub> at boron atoms (B---(OCH <sub>3</sub> ) <sub>4</sub> ) (A) and borohydride (H <sub>(4-x)</sub> B---(OCH <sub>3</sub> ) <sub>x</sub> ) (B).....	62
4.11 Li 1s and B 1s spectra of milled LiBH <sub>4</sub> (A) and nanoconfined	

**LIST OF FIGURES (Continued)**

<b>Figure</b>	<b>Page</b>
LiBH <sub>4</sub> -PMMA-co-BM before desorption (B).....	64
4.12 <sup>11</sup> B NMR of nanoconfined LiBH <sub>4</sub> -PMMA-co-BM before desorption (a), after desorption (b), and after absorption (c).....	67



# CHAPTER I

## INTRODUCTION

### 1.1 Hydrogen Energy

For the last two centuries, coal, crude oil, and natural gas have been consumed by routine life of humans. These fossil fuels have led to a number of environmental problems, for example, global warming caused by greenhouse gas (CO<sub>2</sub>) mainly released from combustion-powered vehicles. Moreover, the high energy consumption has resulted in the reduction of the crude oil supply, which is a critical obstacle for the future developments. Clean energy from fuel cell using hydrogen and oxygen as fuels offers a potential solution to satisfy the global energy requirements because of its properties (clean energy with water as the by-product) as well as a reduction of greenhouse gas emissions. Besides, hydrogen provides high energy density (142 MJ kg<sup>-1</sup>) (Jain et al., 2010), has a great varieties of potential sources (for example, water, biomass, and organic matter (Figure 1.1)), light weight, and has low environmental impact (water is the only by-product from fuel cells using hydrogen as fuel).



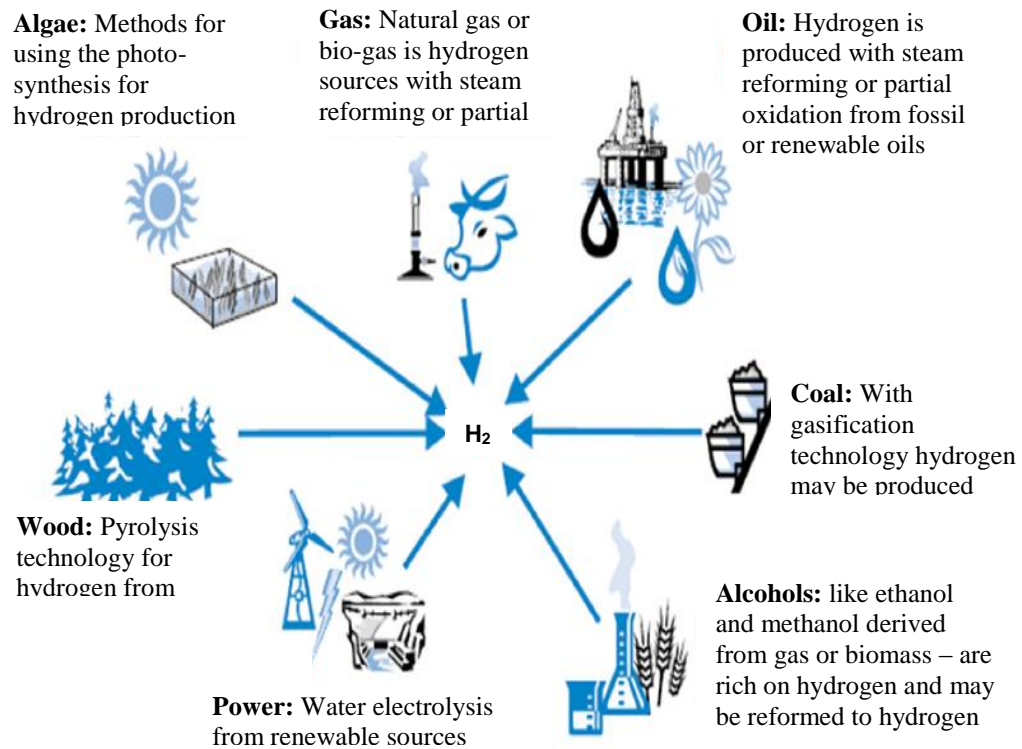
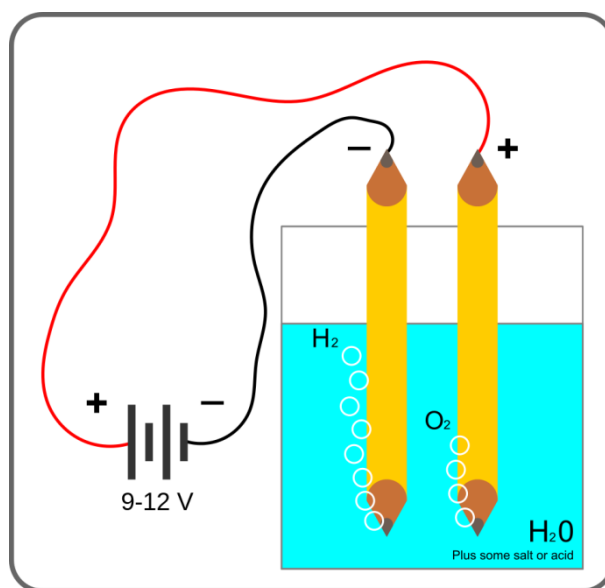


**Figure 1.1** Hydrogen sources. (<http://www.iea.org/publications/freepublications/publication/name,3634,en.html>).

Hydrogen can be produced by steam reforming (Figure 1.2 B) or electrolysis (Figure 1.2 A) methods, but the cost of these processes are quite high and they require energy in the production process. Therefore, scientists are turning to hydrogen production by biological methods or bio-hydrogen (Figure 1.3).

A



B

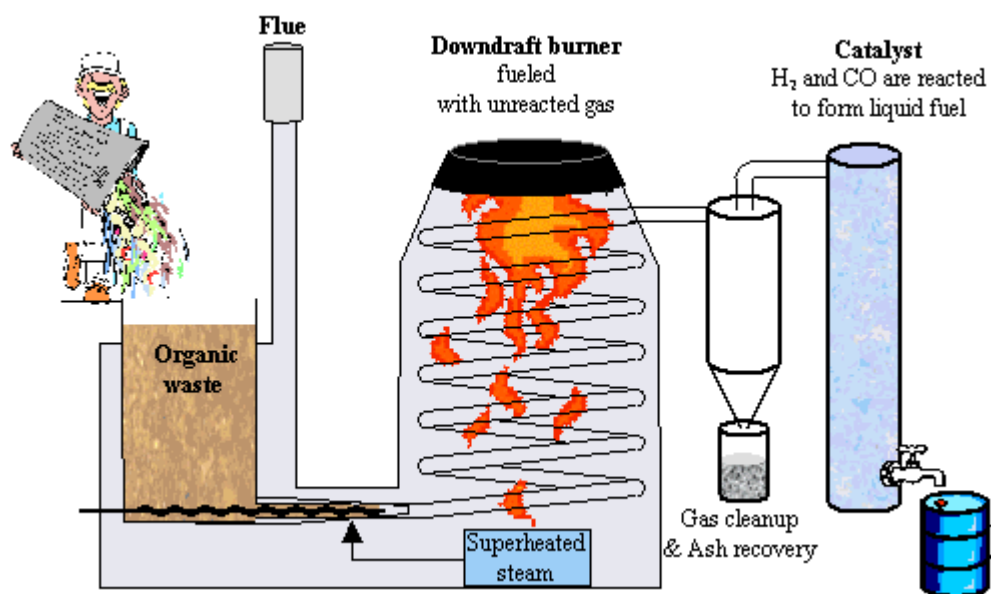


**Figure 1.2** Hydrogen production and processing by electrolysis (A) ([http://en.wikipedia.org/wiki/Electrolysis\\_of\\_water](http://en.wikipedia.org/wiki/Electrolysis_of_water)) and steam reforming (B) (<http://www.thepigsite.com/articles/698/recycle-a-profitable-swine-production-system-with-zero-waste>).

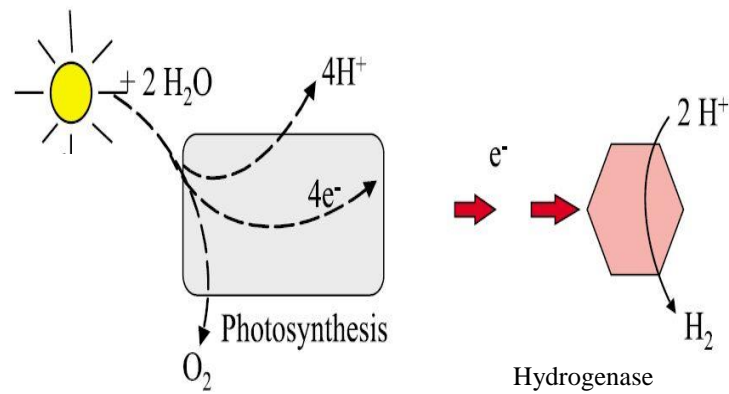


**Figure 1.3** Bio-hydrogen processing cycle (<http://biotech.szbk.u-szeged.hu/h2ase.html>).

Figure 1.3 shows the bio-hydrogen processing cycle. This process is the production of hydrogen by using solar energy. In this process, solar energy is captured by the photosynthetic apparatus, afterward, water is decomposed into oxygen ( $O_2$ ), protons ( $H^+$ ), and electrons ( $e^-$ ). Electrons are delivered to hydrogenase enzyme to create hydrogen. (Microbial Redox Metalloenzyme Research Group, www, 2005).

Hydrogen energy can be used in different applications such as electric power, transportation, industry, and public welfare. Recently, people used hydrogen in fuel cells for transportation applications such as in motor vehicles (Figure 1.4).

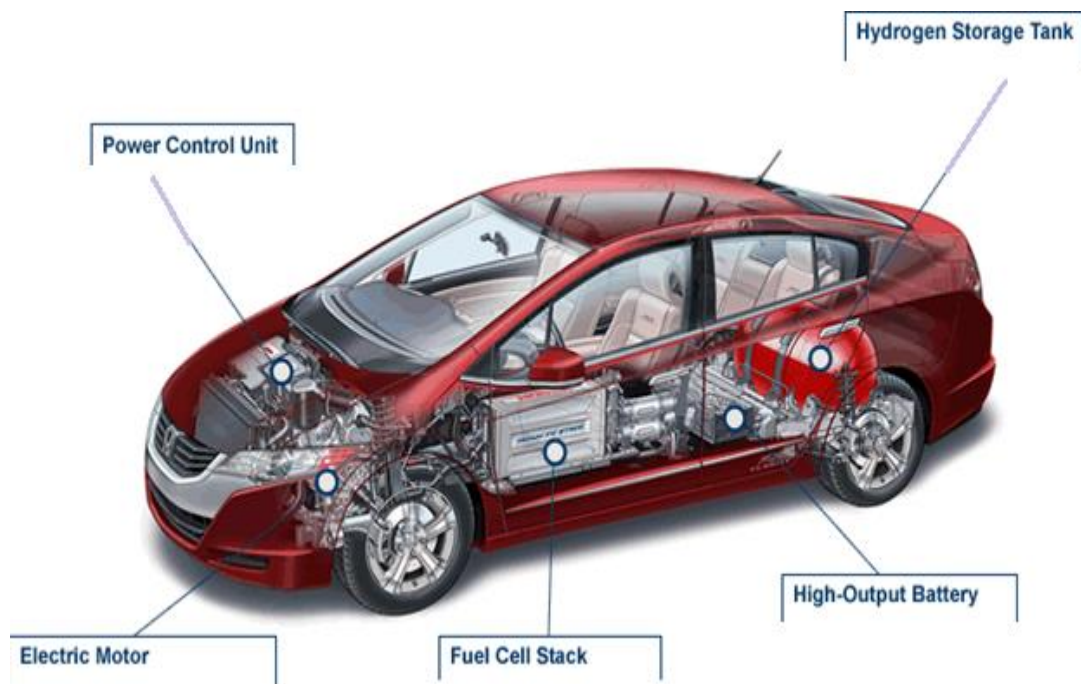


**Figure 1.4** Components of Fuel cell vehicles (FCVs) (<http://www.fueleconomy.gov/feg/fuelcell.shtml>).

A Fuel cell vehicle (FCV) includes three major components (Center for Climate and Energy Solutions, www, 2011) (Figure 1.4):

1. Fuel cell stack: A fuel cell is an electrochemical device that produces electricity using hydrogen and oxygen. To obtain enough electricity to power a vehicle, individual fuel cells are combined in series to make a fuel cell stack.
2. Hydrogen storage tank: The hydrogen gas must be compressed at extremely high pressure at 5,000 to 10,000 pounds per square inch (psi) to store enough fuel to obtain adequate driving range.
3. Electric motor and power control unit: A power control unit governs flow of electricity in the vehicle. By drawing power from either the battery or the

fuel cell stack, it delivers electric power to the motor, which uses the electricity to propel the vehicle.

## 1.2 Fuel Cells

There are several types of fuel cells, each of which is suited for a different application. Fuel cells are typically grouped according to their operating temperature and types of electrolyte used (Table 1.1). The amount of power generated by a fuel cell is determined by several factors including fuel cell type, size, operating temperature, and pressure. The most common type of fuel cell used in FCVs is the polymer electrolyte membrane fuel cells (PEMFCs).

**Table 1.1** Comparison of fuel cell types (U.S. Department of Energy, www, 2011).

Fuel cell types	Electrolytes	Operating temperature (°C)	Applications
Proton exchange membrane fuel cell (PEMFC)	Polymer	60-80	- Transportation - Portable power
Alkaline fuel cell (AFC)	KOH	90-100	- Transportation - Military - Spacecraft - Submarine
Phosphoric acid fuel cell (PAFC)	H <sub>3</sub> PO <sub>4</sub>	175-200	- Transportation - Distributed generation
Solid oxide fuel cell (SOFC)	ZrO <sub>2</sub>	600-1,000	- Distributed generation - Electric utility

Polymer electrolyte membrane fuel cells (PEMFCs) are developed for transportation, stationary power supply, and portable fuel cells. Their distinct features include lower temperature range (50 to 100 °C) and a special polymer electrolyte membrane (Wikipedia, www, 2013).

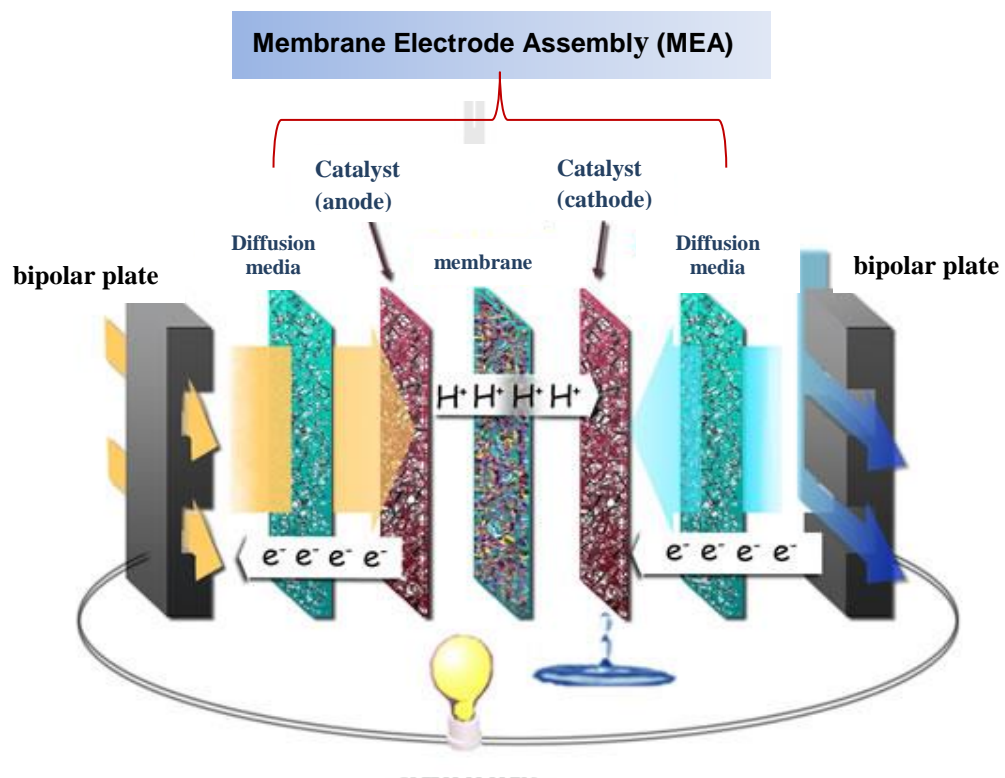


**Figure 1.5** Polymer electrolyte membrane fuel cells (PEMFCs) (<http://newscenter.lbl.gov/feature-stories/2008/04/18/modeling-to-build-a-better-fuel-cell>).

PEMFC is composed of a polymer electrolyte membrane (PEM), electrodes, bipolar plates, and gas diffusion layers (GDL). The PEM placed between an anode (a negative electrode) and a cathode (a positive electrode) by pressure/temperature compression is denoted as a membrane electrode assembly (MEA) (Figure 1.5).

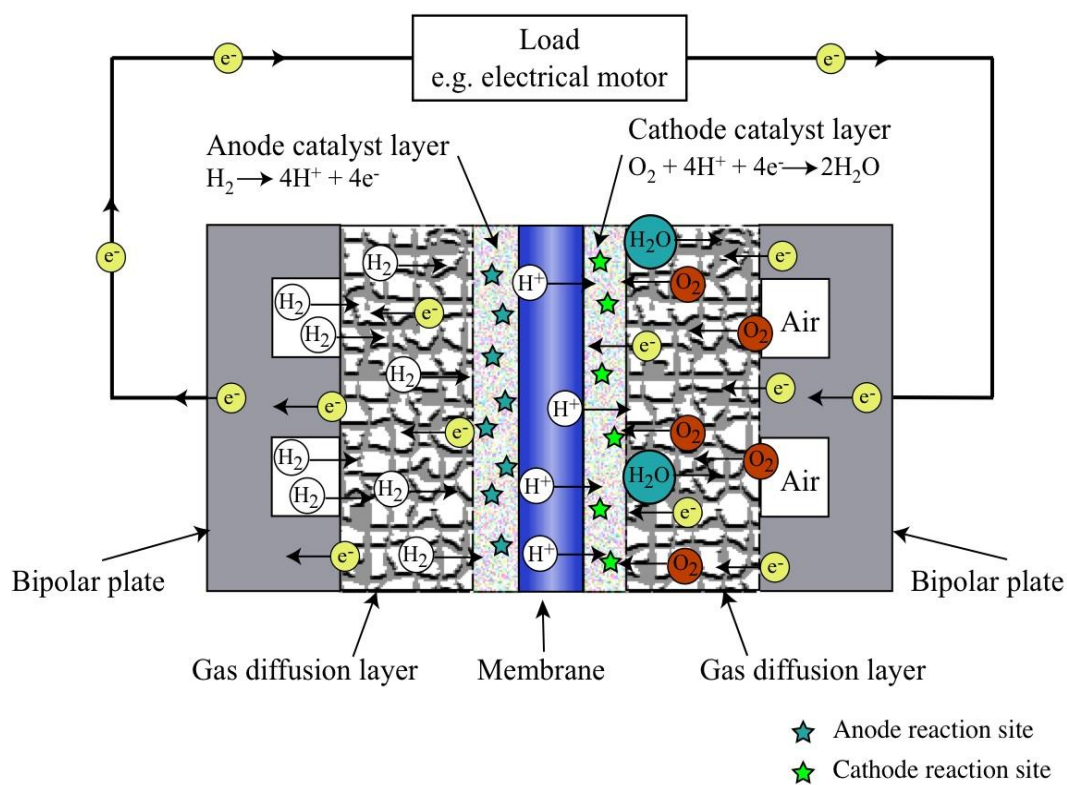


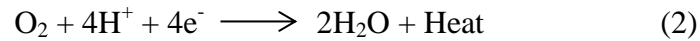
**Figure 1.6** Reaction mechanisms in PEMFC (<http://www.mece.ualberta.ca/groups/energysystemsdesign/research.html>).

From Figure 1.6 (Center for Climate and Energy Solutions, www, 2011), firstly, the hydrogen gas flows to the anode. Here, a platinum catalyst is used to separate the hydrogen molecule into positive hydrogen ions (protons) and negatively charged electrons:

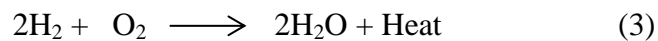


Afterward, the PEM allows only protons to pass through to the cathode, while electrons travel through an external circuit to the cathode. The flow of electrons through this circuit creates the electric current used to power the motor. On the other side of the cell, oxygen gas, usually drawn from the outside air, flows to the cathode.

When electrons return from the external circuit, protons and electrons react with oxygen in the cathode to form water, which then flows out of the cell. The cathode also uses a platinum catalyst to enable this reaction:



Overall reaction:



However, there are three major obstacles for using PEMFCs as energy resources. The first one is the expensiveness of safety as well as the efficiency of hydrogen production. The second problem is the further development of PEMFCs to increase the operating temperature. The last obstacle is hydrogen storage for supplying PEMFCs. From these problems, several attempts try to improve fuel cell technologies, for example, different catalysts and electrolytes are purposed to improve performance and reduce costs. New fuel cell technologies, such as microbial fuel cells, are also studied (Fuel Cells, www, 2000). In the case of hydrogen storage system, three technical systems are currently promising, i.e., (i) compressed hydrogen gas, (ii) liquid hydrogen, and (iii) solid state hydride utilization (Table 1.2).



**Table 1.2** Comparison of three major competing technologies for hydrogen storage (Varin et al., 2009).

Storage system	Volumetric hydrogen capacity ( $\text{kgH}_2 \text{ m}^{-3}$ )	Drawbacks
Compressed hydrogen gas under 80 MPa pressure	~40	<ul style="list-style-type: none"> <li>- safety problem</li> <li>- cost of pressurization</li> <li>- large pressure drop during use</li> </ul>
Liquid hydrogen at cryogenic tank at $-252 \text{ }^\circ\text{C}$ (21 K)	~71	<ul style="list-style-type: none"> <li>- large thermal losses (open system)</li> <li>- safety problem</li> <li>- cost of liquefaction</li> </ul>
Solid state hydrides	80–160	<ul style="list-style-type: none"> <li>- none of the above</li> </ul>

From Table 1.2, major drawbacks of the compressed hydrogen storage for transportation applications are the small amount of hydrogen stored. For compressed hydrogen gas system, it is stored in a reasonable volume and high pressure of 80 MPa is involved in hydrogen gas cylinders, which raises safety concern. There is also some cost involved with compression to such high pressures. Another consideration is the large pressure drop during use.

In case of the use of a liquid hydrogen tank, a higher storage capacity is possible than with pressurized hydrogen. However, major drawbacks of liquid storage are the high cost of the tank for storing the liquid hydrogen. Moreover, large thermal losses for an open system are observed.

The last system is solid state hydrides, which include metal/intermetallic as well as complex hydrides. They have the highest volumetric hydrogen storage

capacities and operate without drawbacks as formed with compressed and liquid hydrogen systems. In addition, the storage tank is smaller than those of compressed and liquid hydrogen (Figure 1.7).

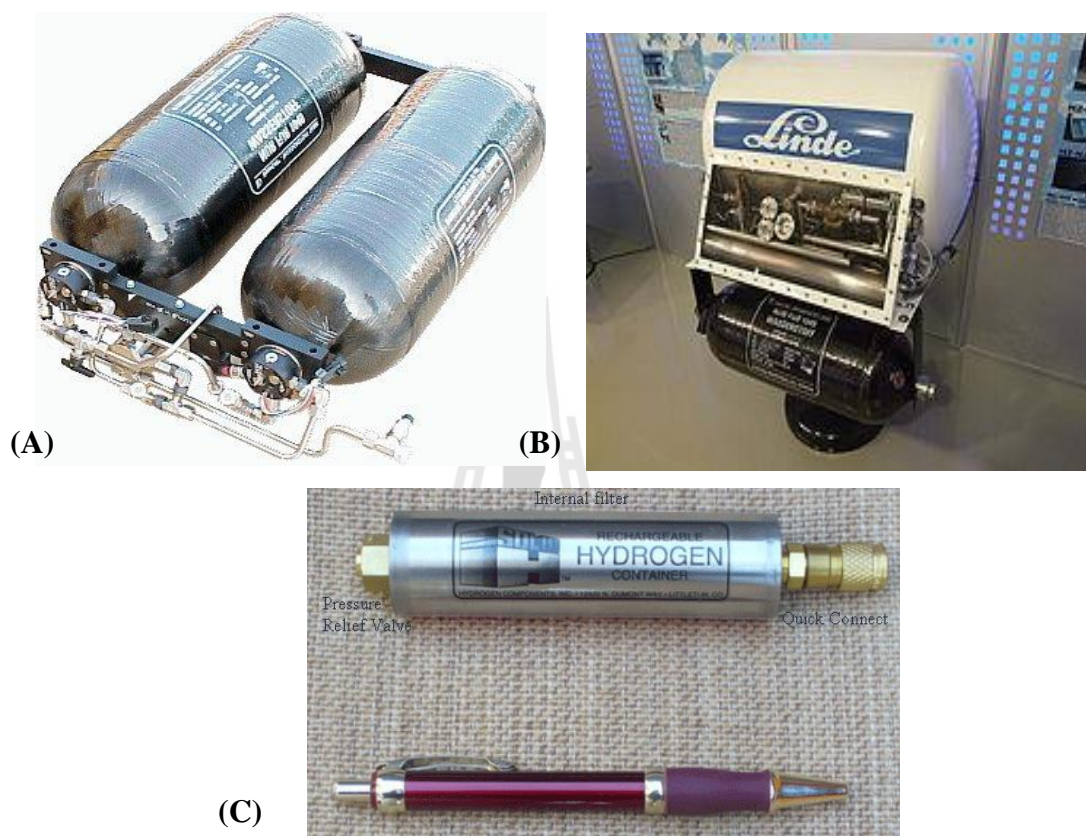


**Figure 1.7** Hydrogen storage tanks of (A) compressed hydrogen gas tank (<http://www.intechopen.com/books/hydrogen-storage/hydrogen-storage-for-energy-application>), (B) liquid hydrogen tank ([http://pl.wikipedia.org/wiki/Linde\\_AG](http://pl.wikipedia.org/wiki/Linde_AG)), and (C) solid state tank (<http://www.hydrogencomponents.com/bl20.html>).

Therefore, several research groups have focused on the solid state hydrides for hydrogen storage application. However, this system still has a lot of obstacles that need to be overcome, including high hydrogen desorption/absorption temperature,

slow hydrogen desorption/absorption kinetics, and release of toxic gases during operation. The technical requirements of hydrogen storage system mentioned by US Department of Energy (US DOE) are listed in Table 1.3.

**Table 1.3** US DOE Freedom CAR hydrogen storage system targets (Varin et al., 2009).

Targeted factor	2007	2010	2015
- Specific energy (MJ kg <sup>-1</sup> )	-	7.2	10.8
- System gravimetric capacity (wt.% H <sub>2</sub> )	4.5	6	9
- System volumetric capacity (kgH <sub>2</sub> m <sup>-3</sup> )	36	45	81
- Energy density (MJ L <sup>-1</sup> )	-	5.4	9.72
- Storage system cost (\$ per kgH <sub>2</sub> )	200	133	67
- System cost (\$ per kg per system)	-	6	3
- Operating temperature (°C)	-20/50	-30/50	-40/60
- Min/max delivery temperature (°C)	-30/85	-40/85	-40/85
- Cycle life-time (absorption/desorption cycles)	500	1,000	1,500
- Flow rate (full throttle) (g s <sup>-1</sup> )	3	4	5
- Delivery pressure from tank to FC (bar)	2.5	2.5	2.5
- Transient response(s) (10–90% and 90–0%)	30	15	15
- Refueling rate (kg H <sub>2</sub> min <sup>-1</sup> )	0.5	1.5	2.0

### 1.3 References

- Berkeley Lab. (2008). **Modeling to Build a Better Fuel Cell** [On-line]. Available: <http://newscenter.lbl.gov/feature-stories/2008/04/18/modeling-to-build-a-better-fuel-cell/>.
- Center for Climate and Energy Solutions. (2011). **Hydrogen Fuel Cell Vehicles** [On-line]. Available: <http://www.c2es.org/technology/factsheet/HydrogenFuelCellVehicles>.
- Energy Efficiency & Renewable Energy. (2014). **Fuel Cell Vehicles** [On-line]. Available: <https://www.fueleconomy.gov/feg/fuelcell.shtml>.
- Energy System Design Laboratory. (2009). **Analysis and Design of Polymer Electrolyte Membrane Electrode Assemblies** [On-line]. Available: <http://www.mece.ualberta.ca/groups/energysystemsdesign/research.html>.
- Fuel cells 2000 (2000). **Types of Fuel Cells** [On-line]. Available: [http://www.fuelcells.org/base.cgim?template=types\\_of\\_fuel\\_cells](http://www.fuelcells.org/base.cgim?template=types_of_fuel_cells).
- InTech-Open Access Company. (2004). **Hydrogen Storage for Energy Application** [On-line]. Available: <http://www.intechopen.com/books/hydrogen-storage/hydrogen-storage-for-energy-application>.
- International Energy Agency. (2006). **Hydrogen Production and Storage** [On-line]. Available: <https://www.iea.org/publications/freepublications/publication/name,3634,en.html>.
- Jain, I.P., Lal, C., and Jain, A. (2010). Hydrogen storage in Mg: A most promising material. **Int. J. Hydrogen Energy**. 35: 5133-5144.
- Microbial Redox Metalloenzyme Research Group (2005). **Hydrogenase** [On-line]. Available: <http://biotech.szbk.u-szeged.hu/h2ase.html>.

Solid-HT<sup>TM</sup> Metal Hydrides. (2009). **Metal Hydride Hydrogen Storage** [On-line].

Available: <http://www.hydrogencomponents.com/bl20.html>.

The Pig Site. (2002). **RE-Cycle: A profitable swine production system with zero waste** [On-line]. Available: <http://www.thepigsite.com/articles/698/recycle-a-profitable-swine-production-system-with-zero-waste>.

U.S. Department of Energy. (2011). **Fuel Cell Technologies Program** [On-line].

Available: <http://www.hydrogenandfuelcells.energy.gov>.

Varin, R. A., Czujko, T., and Wronski, Z. S. (2009). **Nanomaterials for Solid State Hydrogen Storage**. (pp. 3-4). USA: Springer Science and Business Media.

Wikipedia. (2005). **Electrolysis of Water** [On-line]. Available: [http://en.wikipedia.org/wiki/Electrolysis\\_of\\_water](http://en.wikipedia.org/wiki/Electrolysis_of_water).

Wikipedia. (2004). **Liquid Hydrogen** [On-line]. Available: [http://pl.wikipedia.org/wiki/Linde\\_AG](http://pl.wikipedia.org/wiki/Linde_AG).



## CHAPTER II

### LITERATURE REVIEW

Among all hydrogen storage systems, solid state hydrides are the most favorable system in transportation applications, as shown in the comparison in Table 1.2. Therefore, several research groups have attempted to develop these materials for future utilization. There are several metal hydrides, complex hydrides, and composite hydrides, for example, ammonia borane ( $\text{NH}_3\text{BH}_3$ ) and its derivatives (Silvearv, 2011; Sutton et al., 2011; Xiong et al., 2007; Guo et al., 2011), metal aluminium hydrides (e.g.,  $\text{NaAlH}_4$ ,  $\text{Na}_3\text{AlH}_6$ ,  $\text{Na}_2\text{LiAlH}_6$ ) (Bogdanovic and Schwickardi, 1997; Sun et al., 2003; Fu et al., 2006), and metal borohydrides ( $\text{Ca}(\text{BH}_4)_2$ ,  $\text{LiBH}_4$ ) (Rongeat et al., 2010; Gross et al., 2008). One of the most promising materials for hydrogen storage is lithium borohydride ( $\text{LiBH}_4$ ) due to its high gravimetric and volumetric hydrogen densities of 18.5 wt.% and  $121 \text{ kg H}_2/\text{m}^3$ , respectively (Li et al., 2011).

However, dehydrogenation of  $\text{LiBH}_4$  requires high temperature and enthalpy. For dehydrogenation of  $\text{LiBH}_4$ , the main evolution of hydrogen started above  $380 \text{ }^\circ\text{C}$  and only released half of the hydrogen below is  $600 \text{ }^\circ\text{C}$  (Züttel et al., 2003). By the pressure-concentration-temperature (PCT) isotherm measurement, the enthalpy ( $\Delta H$ ) and entropy ( $\Delta S$ ) of dehydrogenation were found to be  $74 \text{ kJ mol}^{-1} \text{ H}_2$  and  $115 \text{ J K}^{-1} \text{ mol}^{-1} \text{ H}_2$ , respectively (Mauron et al., 2008). The hydrogen desorption reaction of  $\text{LiBH}_4$  is reversible, in that the end products of  $\text{LiH}$  and  $\text{B}$  absorb hydrogen at  $600 \text{ }^\circ\text{C}$  and  $35 \text{ MPa H}_2$  to form  $\text{LiBH}_4$ . The absorption reaction requires a long time ( $>12 \text{ h}$ )

and it was not complete (Orimo et al., 2005). These conditions are too high to meet the requirements of the fuel cell operation. Therefore, several approaches have been considered to solve these problems, such as intermetallic compounds, catalytic modifications, reactive hydride composites (RHCs), nanoconfinement in nanoporous scaffolds, and metal hydride polymer composites.

## 2.1 Catalytic Modifications

Orimo et al. (2007) and Nakamori et al. (2006) investigated the thermodynamical stabilities of  $M(\text{BH}_4)_n$  ( $M = \text{Li, Na, K, Cu, Mg, Zn, Sc, Zr}$  and  $\text{Hf}$ ;  $n = 1-4$ ). They found that charge transfer from  $M^{n+}$  to  $[\text{BH}_4]^-$  is a key factor for the stability of  $M(\text{BH}_4)_n$  and it reveals a linear relationship between the calculated formation enthalpy ( $\Delta H$ ) of  $M(\text{BH}_4)_n$  and the Pauling electronegativity ( $\chi_P$ ) of  $M$ . The thermal desorption temperature ( $T_d$ ) of  $M(\text{BH}_4)_n$  was closely correlated with  $\chi_P$ . That is,  $T_d$  decreases with increasing values of  $\chi_P$ . However, in the case of  $M(\text{BH}_4)_n$  with a single cation  $M^{n+}$ , regular adjustment of  $T_d$  might be difficult due to natural and discrete value of  $\chi_P$  for each metal. For this reason, an approach of producing multi-cation borohydrides  $MM'(\text{BH}_4)_m$ , in which  $M$  and  $M'$  have different electronegativity, has been proposed to precisely tailor the thermodynamic stability. Yang et al. (2007) modified  $\text{LiBH}_4$  by ball-milling with  $\text{Al}$  or  $\text{Al}$  containing compounds. During cycling,  $\text{AlB}_2$  was formed in the dehydrogenated state and disappeared in the hydrogenated state. The formation of  $\text{AlB}_2$  decreases the stability of the materials and thus results in a lower desorption temperature. Kang et al. (2007) found that  $\text{LiBH}_4\text{-Al}$  system possessed a theoretical capacity of 8.5 wt.% and could be reversibly operated at 400–

450 °C. Moreover, the influences of additive ( $\text{TiF}_3$ ) on  $\text{LiBH}_4\text{-Al}$  sample were also investigated (Figure 2.1).

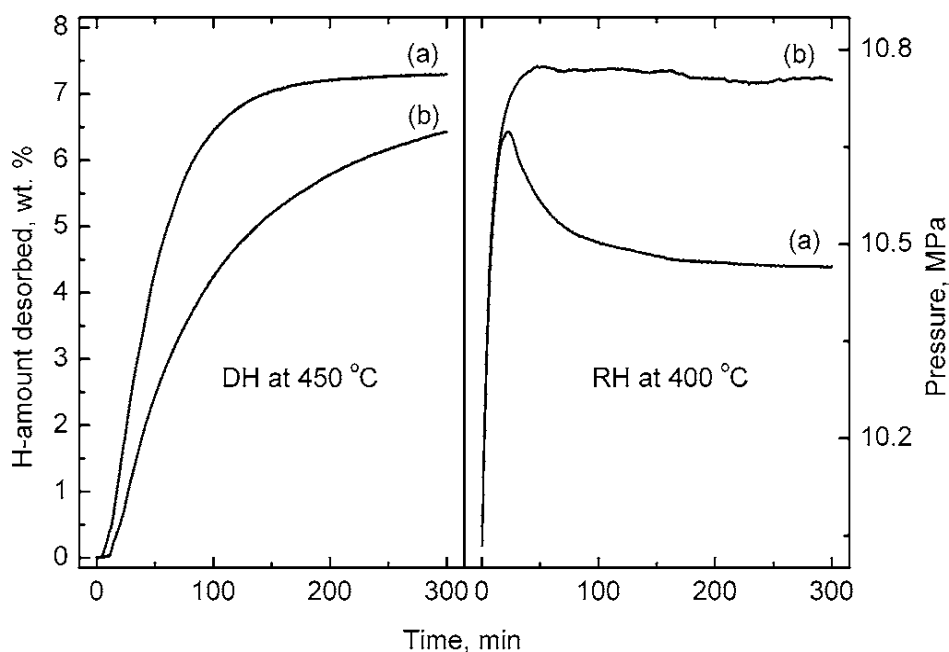


**Figure 2.1** Dehydrogenation (DH)/rehydrogenation (RH) profiles of (a)  $\text{LiBH}_4+1/2\text{Al}+0.04\text{TiF}_3$  and (b)  $\text{LiBH}_4+0.04\text{TiF}_3$  (Kang et al., 2007).

From Figure 2.1, the sample of  $\text{LiBH}_4+1/2\text{Al}+0.04\text{TiF}_3$  is observed to release over 7.2 wt.%  $\text{H}_2$  in ~ 3 h at 450 °C, while that of  $\text{LiBH}_4+0.04\text{TiF}_3$  releases only 5.5 wt.%  $\text{H}_2$  under identical measurement conditions. Interestingly, it was found that the addition of Al favored reversible rehydrogenation at relatively moderate conditions (10 MPa hydrogen at 400 °C) (Kang et al., 2007).

Another approach to improve the kinetics of hydrogen absorption and desorption is the use of catalysts. The experimental results show that additives, such as  $\text{TiO}_2$ ,  $\text{TiCl}_3$ ,  $\text{TiF}_3$ , and  $\text{MgCl}_2$  (Kang et al., 2007; Au et al., 2006; Vajo et al., 2007;



Au et al., 2008) are effective in reducing the dehydrogenation temperature. The lowest onset temperature for dehydrogenation started at 60 °C for  $\text{LiBH}_4+0.2\text{MgCl}_2+0.1\text{TiCl}_3$  sample. It desorbed 5 wt.%  $\text{H}_2$  at 400 °C and absorbed 4.5 wt.%  $\text{H}_2$  at 600 °C under the pressure of 7 MPa  $\text{H}_2$  (Au et al., 2008; Au et al., 2006).

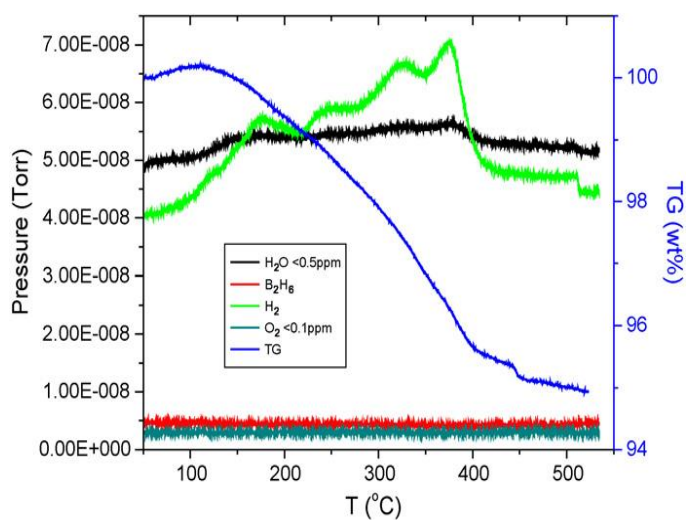


**Figure 2.2** TGA and RGA spectra of the material  $\text{LiBH}_4+0.2\text{MgCl}_2+0.1\text{TiCl}_3$  (Au et al., 2008).

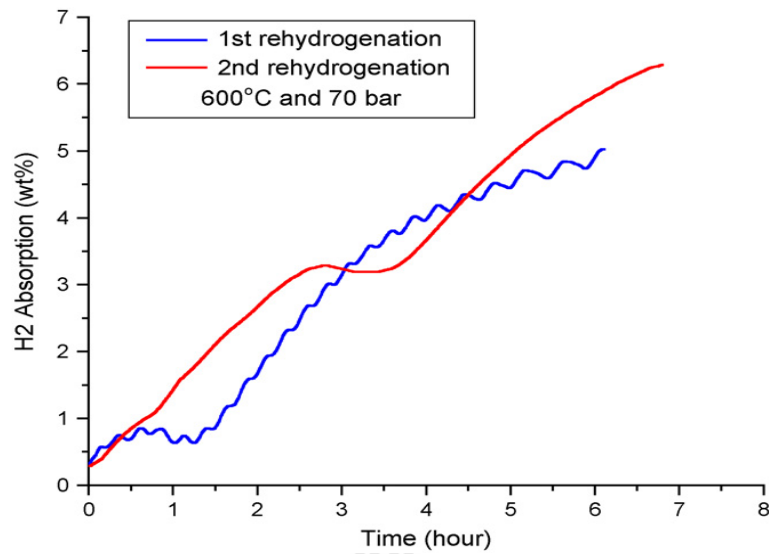


**Figure 2.3** Isothermal rehydrogenation of the material  $\text{LiBH}_4+0.2\text{MgCl}_2+0.1\text{TiCl}_3$  (Au et al., 2008).

From Figure 2.2, the sample started releasing hydrogen at 60 °C together with the total amount of hydrogen released of 5 wt.% at 400 °C during the first cycle. Thereafter, dehydrogenated sample of  $\text{LiBH}_4+0.2\text{MgCl}_2 +0.1\text{TiCl}_3$  absorbed 5 wt.%  $\text{H}_2$  at 600 °C and 70 bar  $\text{H}_2$  (Figure 2.3). In the case of the second cycle, 6.3 wt.%  $\text{H}_2$  is absorbed under similar condition as in the first cycle (Figure 2.3).

## 2.2 Reactive Hydride Composites (RHCs)

A typical example for destabilization of  $\text{LiBH}_4$  is the reactive composite hydride of  $2\text{LiBH}_4-\text{MgH}_2$ . Vajo et al. (2005; 2007a; 2007b) reported enhanced hydrogen sorption properties when  $\text{MgH}_2$  was added to  $\text{LiBH}_4$ . The formation of  $\text{MgB}_2$  upon dehydrogenation reduced the de-/rehydrogenation enthalpy by 25 kJ/ (mol of  $\text{H}_2$ ) compared with pure  $\text{LiBH}_4$ . The reversibility was also improved.

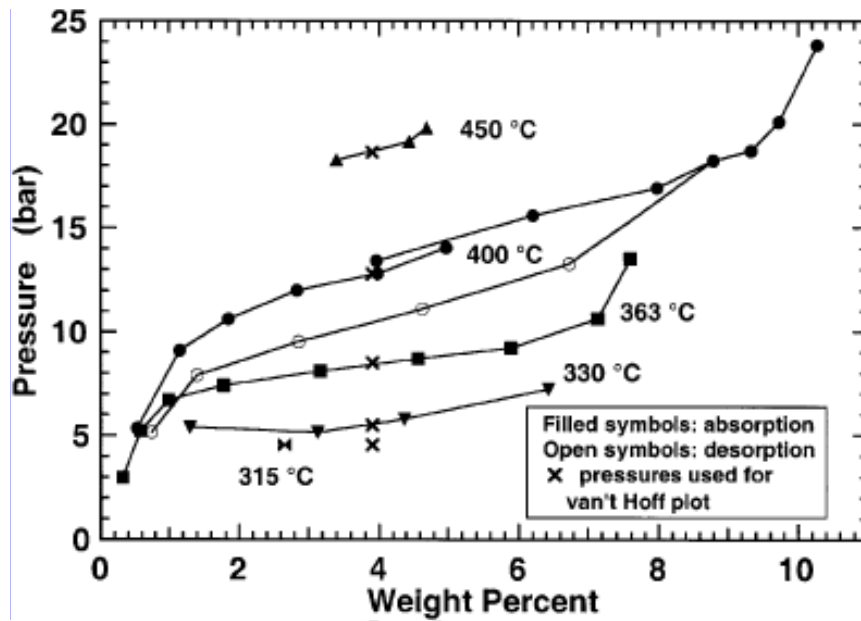


**Figure 2.4** Absorption/desorption isotherms at 315-450 °C for the  $\text{LiBH}_4 + 1/2\text{MgH}_2$  system (Vajo and Skeith, 2005).

From Figure 2.4, the isotherms show sloping plateaus from 2 to 8 wt.% with capacity of approximately 10 wt.%. Equilibrium pressures varied from 4.5 bar at 315 °C to 19 bar at 450 °C. A preliminary van't Hoff plot (logarithm of the equilibrium pressure versus the inverse of the absolute temperature) using absorption equilibrium pressures at 4 wt.% (Figure 2.4) is shown in Figure 2.5.

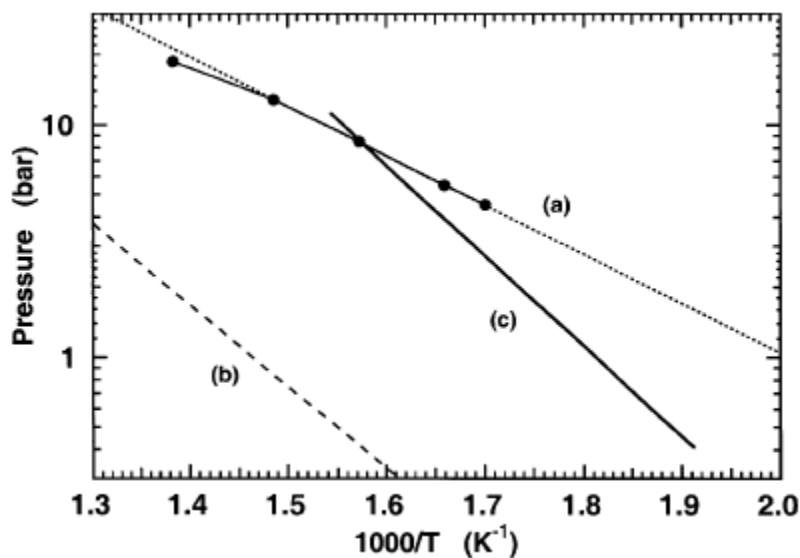


**Figure 2.5** Van't Hoff plots of destabilized (a)  $\text{LiBH}_4+1/2\text{MgH}_2$ , (b) pure  $\text{LiBH}_4$ , and (c)  $\text{MgH}_2$  (Vajo and Skeith, 2005).

Figure 2.5, curve (a) shows equilibrium pressures obtained from the absorption isotherms at 4 wt.% in Figure 2.4. A linear fit to the data at 315-400 °C indicates a dehydrogenation enthalpy of 40.5 kJ/ (mol of  $\text{H}_2$ ) and an equilibrium pressure of 1 bar at 225 °C. Curve (b) reveals an estimate of the behavior for dehydrogenation of  $\text{LiBH}_4$  to  $\text{LiH} + \text{B}$ . Curve (c) shows the equilibrium pressure for  $\text{MgH}_2/\text{Mg}$ . Addition of  $\text{MgH}_2$  increases the equilibrium pressure by approximately 10 times while lowering the enthalpy by 25 kJ/(mol of  $\text{H}_2$ ) compared with pure  $\text{LiBH}_4$ .

Bösenberg et al. (2007) found that at high temperatures and low pressures, independent decomposition of all hydrides ( $\text{LiBH}_4$  and  $\text{MgH}_2$ ) and subsequent formation of  $\text{MgB}_2$  were observed. The system with catalytic doping ( $2\text{LiBH}_4\text{-MgH}_2\text{-5 wt. \% TiO}_2$ ) was also studied.

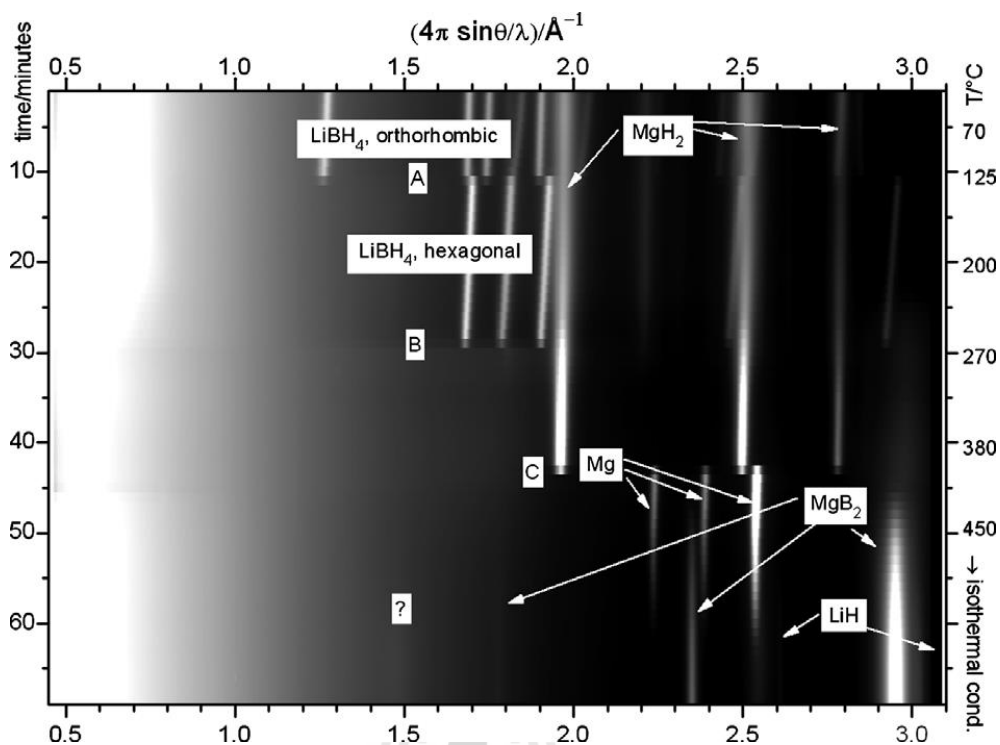
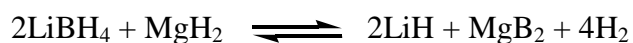


**Figure 2.6** In situ XRD measurement of the desorption reaction of 2LiBH<sub>4</sub>–MgH<sub>2</sub> composite doped with 5 wt. % titanium isopropoxide (Bösenberg et al., 2007).

Figure 2.6 shows the results of the desorption reaction under a hydrogen pressure of 5 bar. Phase transformation from *o*-LiBH<sub>4</sub> to *h*-LiBH<sub>4</sub> and melting of *h*-LiBH<sub>4</sub> occur at around 120 and 270 °C, respectively. Desorption of MgH<sub>2</sub> to Mg occurs at about 390 °C. After the formation of Mg, MgB<sub>2</sub> forms at temperatures above 400 °C. At the same time, the Mg diffraction intensities decrease. Desorption of LiBH<sub>4</sub> can be confirmed by the formation of MgB<sub>2</sub> and LiH. Therefore, the dehydrogenation reaction mechanism of 2LiBH<sub>4</sub>–MgH<sub>2</sub> composite (11.6 wt.%) is as the following reaction:



However, it should be noted that the desorption temperature (350 °C) was still high, although the system was modified with additive (400 °C). Thus, other strategies still must be investigated.

### 2.3 Nanoconfinement in Nanoporous Scaffolds

The nanoengineering to confine light metal hydrides in the nanoporous scaffold was carried out to improve kinetics and to decrease the dehydrogenation temperature. The shorter diffusion distances for hydrogen and the other light elements nanoconfined in the scaffold result in faster net rates for hydrogenation and dehydrogenation. Ngene et al. (2010) investigated the confinement of  $\text{LiBH}_4$  in an ordered mesoporous  $\text{SiO}_2$  (SBA-15) and its effects on the hydrogen sorption properties. They demonstrated that  $\text{LiBH}_4$  could fully fill the mesopores of SBA-15 under hydrogen pressure, while the long-range order of the mesopores was maintained. The confined  $\text{LiBH}_4$  has enhanced hydrogen desorption properties with desorption starting at 150 °C. However, upon dehydrogenation,  $\text{SiO}_2$  and decomposition products of  $\text{LiBH}_4$  reacted to form  $\text{Li}_2\text{SiO}_3$  and  $\text{Li}_4\text{SiO}_4$ , leading to irreversible hydrogen loss. Zhang et al. (2007) reported that  $\text{LiBH}_4$  nanoparticles supported by disordered mesoporous carbon CMK-3 showed favorable latent heat of dehydrogenation (40 kJ/mol  $\text{H}_2$ ), large amount of dehydrogenation capacity (14 wt.%) below 600 °C, and reversible capacity of 6.0 wt.%  $\text{H}_2$  at 350 °C. Furthermore, Gross et al. (2008) found that the enhancement of kinetics for hydrogen exchange in  $\text{LiBH}_4$  was observed when  $\text{LiBH}_4$  was incorporated in nanoporous carbon scaffold. Moreover, the activation energy for hydrogen desorption decreased from 146 kJ/mol to 103 kJ/mol after nanoconfinement. In 2010, Liu et al. investigated desorption of

LiBH<sub>4</sub> in the presence of highly ordered nanoporous carbon. LiBH<sub>4</sub> was found in amorphous state in nanopores. The confinement of LiBH<sub>4</sub> reveals the disappearance of phase transformation and melting of LiBH<sub>4</sub>, and the decrease of the onset desorption temperature from 460 to 220 °C.

Moreover, the effects of nanoconfinement on desorption of LiBH<sub>4</sub> had been investigated in the presence of various porous hard carbon templates at a variety of pore sizes. Calorimetric signatures of both the structural phase transition and melting of nanoconfined LiBH<sub>4</sub> shifted to a lower temperature with respect to the bulk material. In addition, the desorption temperature of LiBH<sub>4</sub> confined in these nanoporous carbons obviously decreased. Mass spectroscopic analysis also indicated a gradual reduction of B<sub>2</sub>H<sub>6</sub>, which could poison the fuel cell catalyst, with decreasing pore size. This suggests that formation of the very stable [B<sub>12</sub>H<sub>12</sub>]-based closoborane salts, which represent thermodynamic sinks and significantly reduce the capacity and reversibility of borohydride-based materials, can be largely moderated by the nanoconfinement of the hydride (Lui et al., 2011).

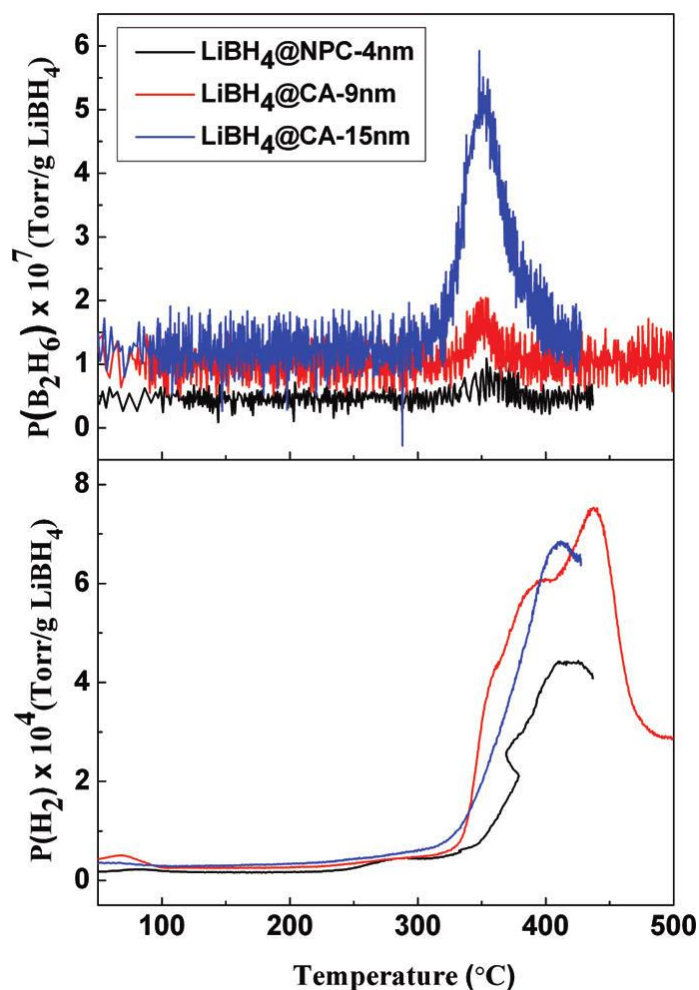


**Figure 2.7**  $B_2H_6$  and  $H_2$  release at various temperatures of  $LiBH_4$  nanoconfined in porous carbon (NPC) 4 nm ( $LiBH_4@NPC-4$  nm), in carbon aerogel (CA) 9 nm ( $LiBH_4@CA-9$  nm), and in CA-15 nm ( $LiBH_4@CA-15$  nm). The loading of each sample is 10 wt. % (Lui et al., 2011).

From Figure 2.7, more  $B_2H_6$  is released from the decomposition of  $LiBH_4@CA-15$  nm and  $LiBH_4@CA-9$  nm than  $LiBH_4@NPC-4$  nm, where the only small release of  $B_2H_6$  is obtained.



During hydrogen desorption reaction, the chemistry of sample changed.

Therefore, the chemical concentrations and interactions resulted in early diborane formation changing, which enough to reduce the amount of diborane production. The partial pressures and amount of infiltrated hydride, indicate that the amount of diborane released during the decomposition of  $\text{LiBH}_4$  decreases with decreasing pore size, and nanoconfinement can suppress or eliminate the reaction path that produces  $\text{B}_2\text{H}_6$ .

Furthermore,  $\text{LiBH}_4$  and  $\text{MgH}_2$  nanoparticles were embedded in a nanoporous carbon aerogel scaffold of resorcinol-formaldehyde aerogel with 21 nm pore sized by di-n-butylmagnesium ( $\text{MgBu}_2$ ) precursor and molten  $\text{LiBH}_4$  infiltration.  $\text{LiBH}_4$  and  $\text{MgH}_2$  reacted during dehydrogenation to form  $\text{MgB}_2$ . The hydrogen desorption kinetics was significantly improved as compared to bulk material and the nanoconfined system has a high degree of reversibility and stability and possibly also improved thermodynamic properties (Nielsen et al., 2010). Afterward, Gosalawit-Utke et al. (2011) prepared nanoconfined  $2\text{LiBH}_4\text{-MgH}_2$  by direct melt infiltration of bulk  $2\text{LiBH}_4\text{-MgH}_2$  into an inert nanoporous resorcinol-formaldehyde carbon aerogel scaffold material. A significant improvement in hydrogen desorption kinetics as compared to bulk  $2\text{LiBH}_4\text{-MgH}_2$  was obtained.

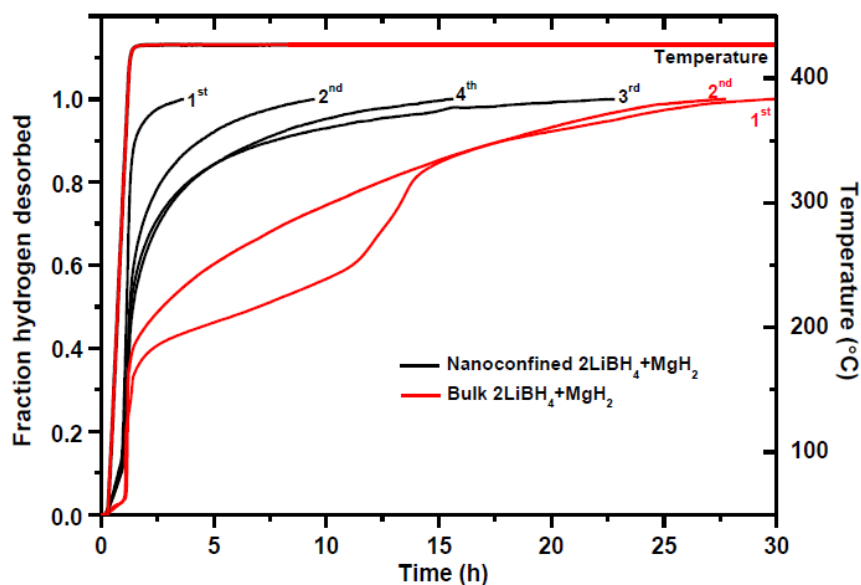


**Figure 2.8** Normalized hydrogen desorption profiles of the nanoconfined  $2\text{LiBH}_4\text{-MgH}_2$  and bulk  $2\text{LiBH}_4\text{-MgH}_2$  (Gosalawit-Utke et al., 2011).

Figure 2.8 shows that the hydrogen desorption rate of the nanoconfined  $2\text{LiBH}_4\text{-MgH}_2$  is considerably higher as compared to bulk material, for example, 90% of the total hydrogen content in the nanoconfined  $2\text{LiBH}_4\text{-MgH}_2$  release after 1.5 h during the first cycle, whereas the bulk material release only 34%. Furthermore, it also shows the faster kinetics of the nanoconfined  $2\text{LiBH}_4\text{-MgH}_2$  over the bulk material even after four hydrogen release and uptake cycles. And a reversible gravimetric hydrogen storage capacity of 10.8 wt.%  $\text{H}_2$ , which was calculated with respect to the metal hydride content, was preserved over all cycles.

However, there are still some important disadvantages of metal hydride confined in a carbon host; i.e., (1) high temperature and pressure for dehydrogenation and rehydrogenation and (2) oxidation of metal hydrides. Therefore, new host materials for nanoconfinement are of interest not only to improve kinetics, but also to

prevent deterioration of hydride materials from air and humidity.

## 2.4 Metal Hydride Polymer Composites

Polymers are among the most suitable materials to solve this problem due to their hydrophobic property. In the case of hydrogen sorption, a polymer can store hydrogen via both physical and chemical mechanisms. Germain et al. (2006) reported physical hydrogen adsorption of nanoporous polymer (hypercrosslinked Hypersol-Macronet MN200 resin). They found that the higher the surface area, the greater amount of hydrogen was adsorbed. The maximum hydrogen storage capacity of 1.3 wt.% at 77.3 K was obtained. Afterward, Jurczyk et al. (2007) investigated the polyaniline-based nanocomposite materials for hydrogen storage. They found that there is interaction between polymer matrix of polyaniline and hydrogen during hydrogen sorption (Figure 2.9).

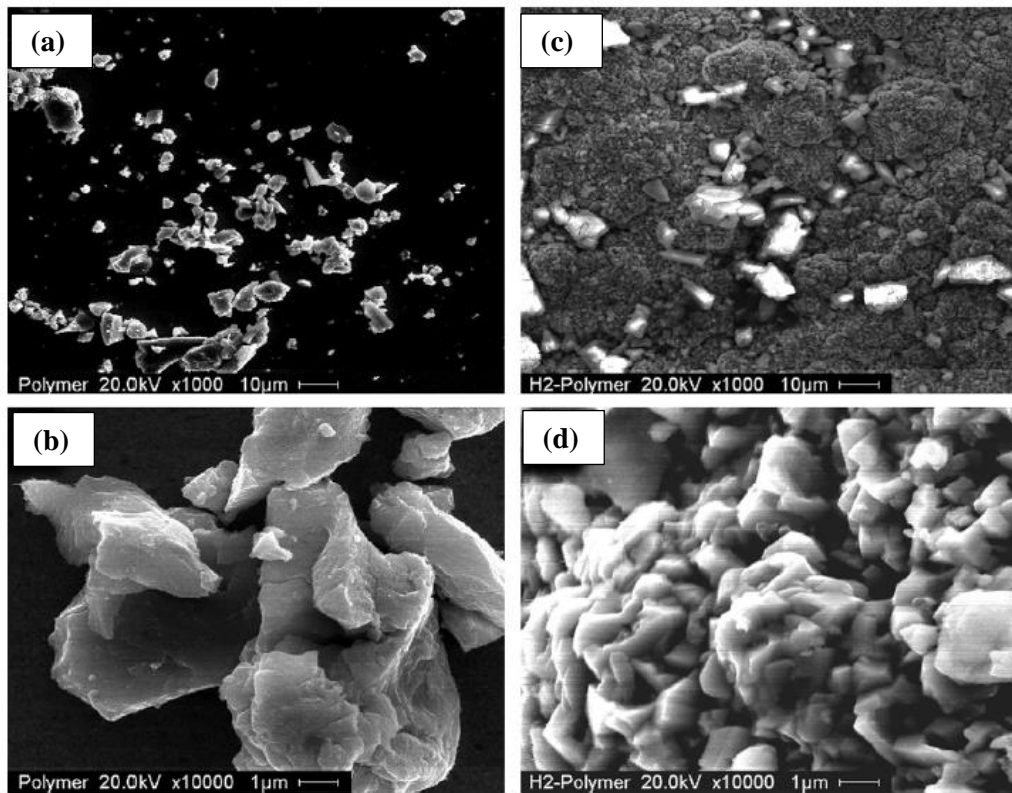


**Figure 2.9** SEM images of standard polyaniline before ((a) and (b)) and after hydrogen sorption ((c) and (d)). (Jurczyk et al., 2007).

As shown in Figures 2.9 (a) and (b), they clearly exhibit a rough surface the polyaniline. After hydrogen adsorption (Figure 2.9 (c) and (d)), the polymer–hydrogen interaction results in a ballooning effect, in which the hydrogen was stored in small pockets. This indicates that the hydrogen is stored physically rather than chemically. Moreover, the addition of aluminum to the nanocomposite increases the hydrogen sorption due to the chemical interaction between aluminum and polyaniline (Figure 2.10).

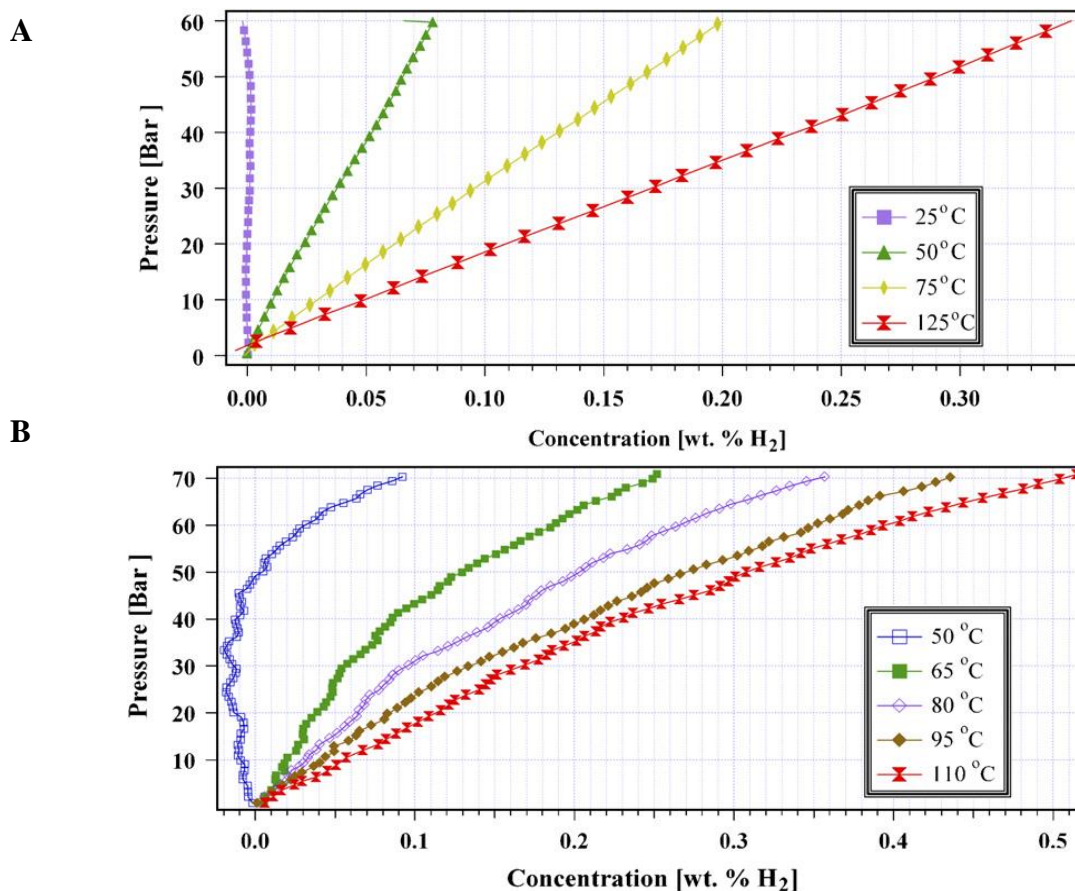


**Figure 2.10** Hydrogen sorption measurements of polyaniline (A) and polyaniline with 30 wt. % aluminum powder (B) at different temperatures and increasing pressure (Jurczyk et al., 2007).

In Figure 2.10, it can be seen that this nanocomposite material exhibits a much higher hydrogen sorption than the polyaniline sample. It is interesting to note that hydrogen sorption begins at 50 °C, at above approximately 50 bar hydrogen pressure with higher hydrogen capacity as compared to 50 °C for polyaniline sample. Furthermore, Srinivasan et al. (2010) synthesized electrospun polyaniline fibers for hydrogen adsorption. Figure 2.11 shows that the reversible hydrogen storage capacity of ~3–10 wt. % is observed in the temperature range of 50–125 °C.

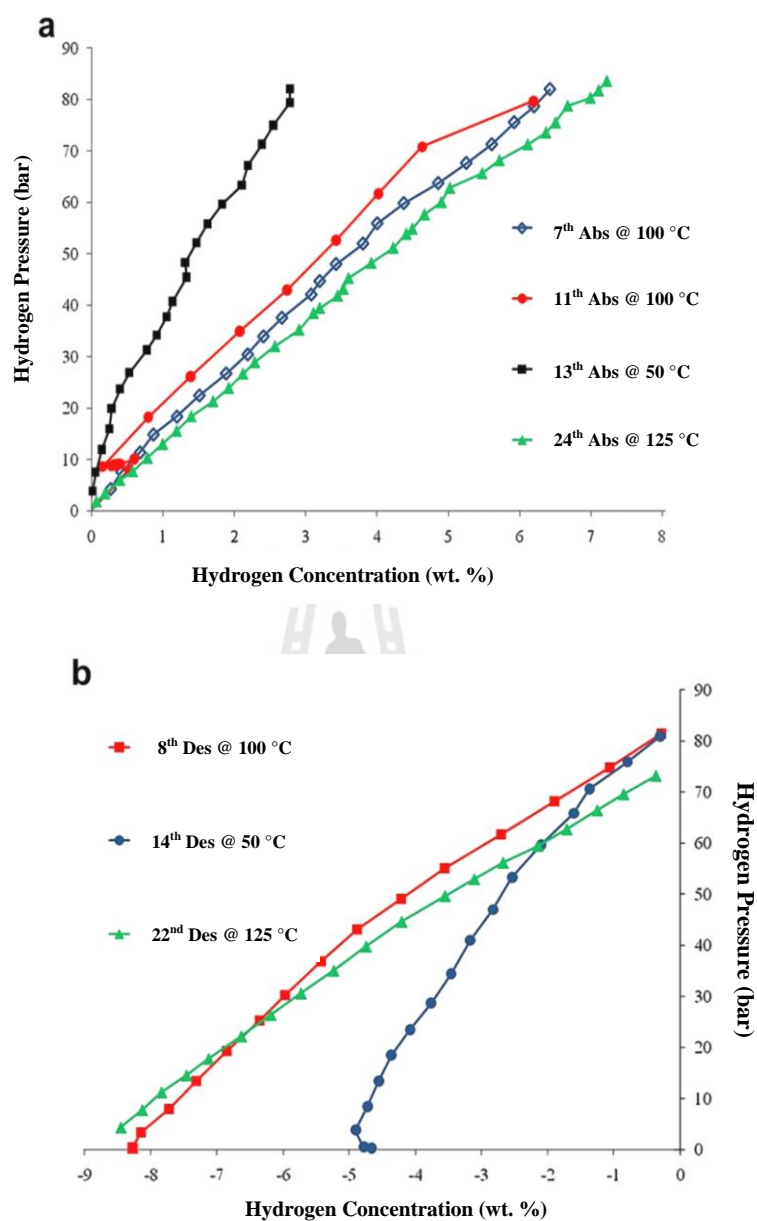


**Figure 2.11** Hydrogen (a) adsorption and (b) desorption PCT curves for polyaniline fibers (Srinivasan et al., 2010).

From Figure 2.11 (a), at lower temperature of 50 °C, a hydrogen capacity of 3 wt.% is obtained, while at 100–125 °C, hydrogen capacity increases to 6–8 wt.%. In the case of desorption, a hydrogen storage capacity of 2–8 wt.% is obtained at

temperature range of 50–125 °C (Figure 2.11(b)). This may be explained by changes of surface morphology before and after hydrogen sorption (Figure 2.12).

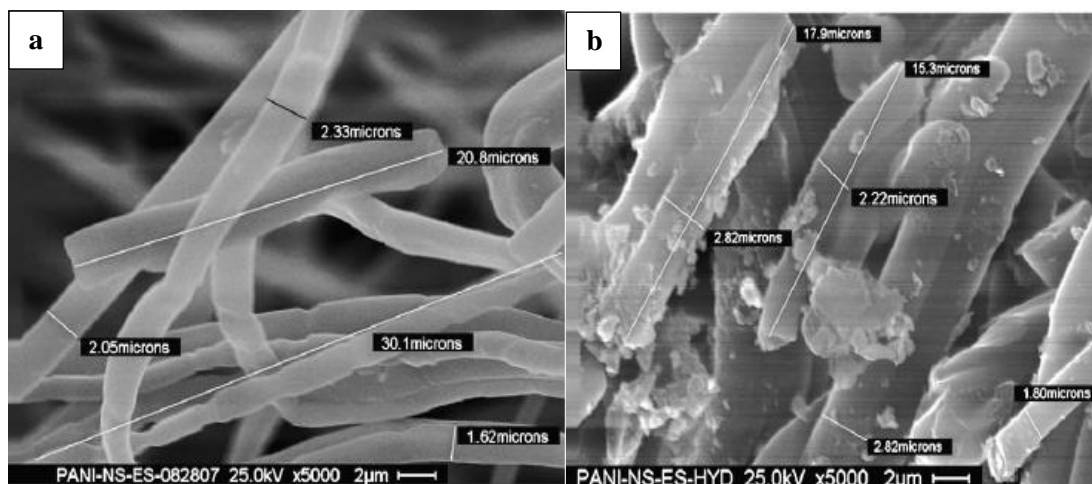


**Figure 2.12** SEM micrographs of polyaniline fibers before (a) and after hydrogen sorption (b) cycles (Srinivasan et al., 2010).

Figure 2.11 (a) reveals the length of fiber formation. After hydrogen sorption cycles, sample exhibits fibrillar swelling, breaking of fiber length, and precipitations of sample. Therefore, the high volumetric hydrogen storage capacities (3–10 wt.%) in polyaniline fibers may be explained on the basis of morphological swelling due to hydrogen interaction on the surface and in bulk of sample.

In the case of chemical absorption, hydrogen is stored in the form of hydride solid powder, e.g. metal hydrides and complex hydrides. Checchetto et al. (2009) synthesized metal-polymer composites of LaNi<sub>5</sub> and Pd with hydrogen permeable polymers of polyethylene (PE), polysiloxane (PS), and polyvinyl pyrrolidone (PVP). Faster kinetics were obtained from PS–LaNi<sub>5</sub> and PVP–Pd. Nevertheless, metal particle agglomeration in both samples was investigated (Figure 2.13).

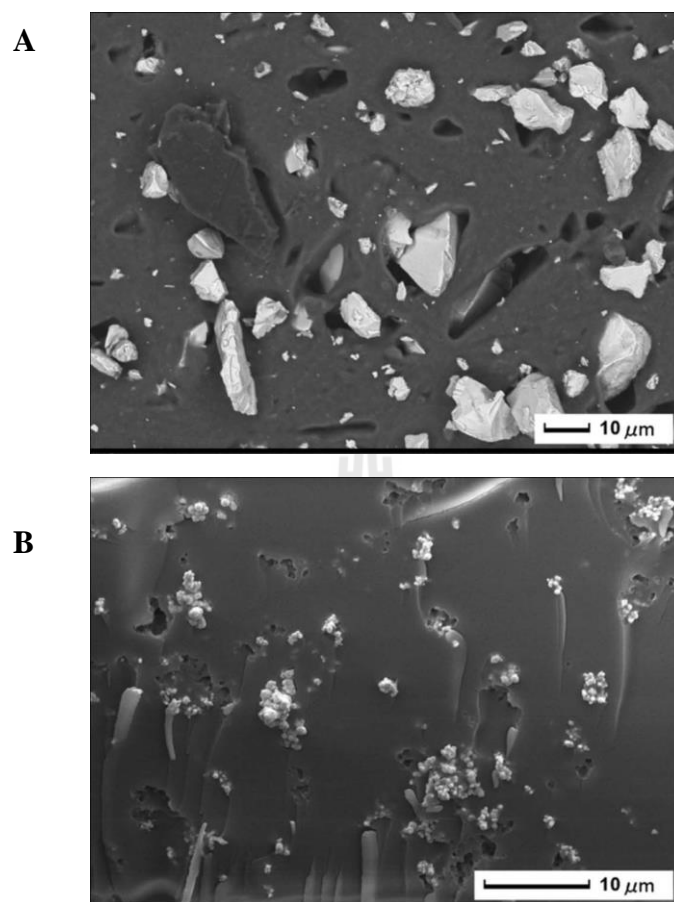


**Figure 2.13** SEM micrographs of as prepared PS-LaNi<sub>5</sub> (A) and PVP-Pd (B) composites (Checchetto et al., 2009).

Interestingly, Jeon et al. (2011) reported the synthesis of an air-stable composite material consisting of metallic Mg nanocrystals (NCs) in a gas-barrier polymer matrix that enabled both the storage of a high density of hydrogen (up to 6 wt. % with respect to MgH<sub>2</sub> content) and rapid kinetics (5.97 wt. % H<sub>2</sub> within < 30 minute) without using expensive heavy-metal catalysts (T=200 °C and  $p(\text{H}_2) = 35$  bar H<sub>2</sub>). Figure 2.14 shows a high H<sub>2</sub>/O<sub>2</sub> permeability of PMMA polymer matrix (ratio of 42.9 at 35 °C) and also protection of MgH<sub>2</sub> from air and oxygen (Jeon et al., 2011).



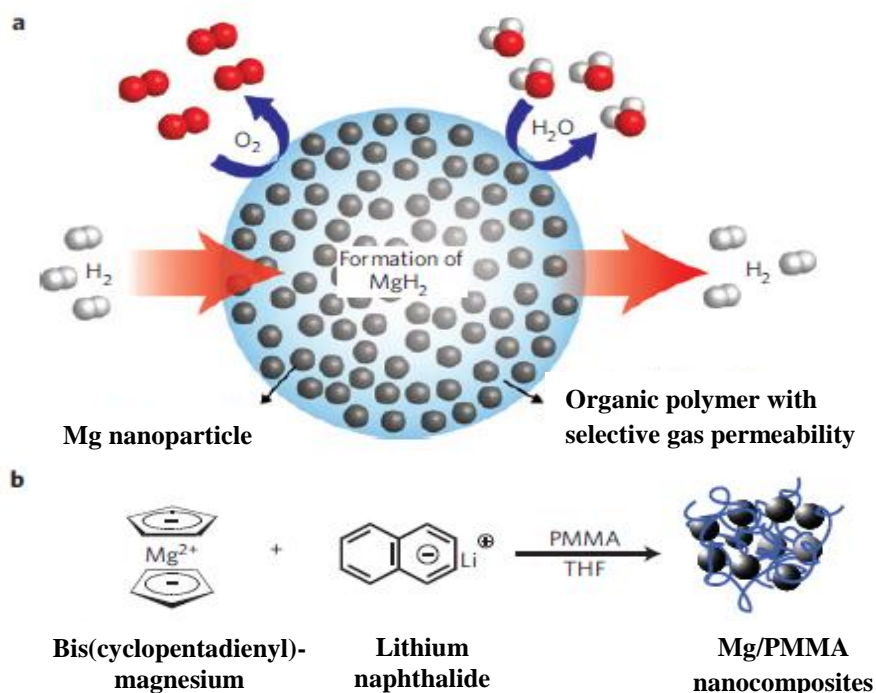


**Figure 2.14** Mg NCs in a gas-barrier polymer matrix (Jeon et al., 2011).

On the basis of the hydrophobic surface and amorphous structure of poly (methyl methacrylate) (PMMA) (Figure 2.15 (A)), nanoconfinement of  $LiBH_4$  in PMMA is hypothesized not only to avoid the deterioration of  $LiBH_4$  by oxygen and humidity, but also to provide high  $H_2$  permeability and/or a pathway for the hydrogen exchange reaction of  $LiBH_4$ . In this work, we prepare nanoconfined  $LiBH_4$  via solution impregnation in a PMMA derivative of poly (methyl methacrylate)-co-butyl methacrylate (PMMA-co-BM) (Figure 2.15 (B)) for reversible hydrogen storage. On the basis of a butyl-branched chain, PMMA-co-BM has a superior amorphous degree as compared to pure to PMMA, leading to higher free volume in the polymer matrix for  $H_2$  permeability. In addition, nanoparticles of  $LiBH_4$  can be homogeneously embedded

in the PMMA-co-BM polymer matrix via solution impregnation.

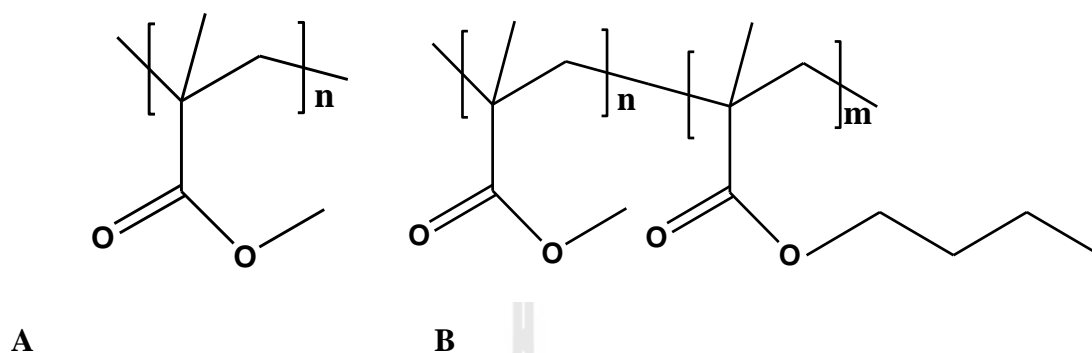


**Figure 2.15** Chemical structures of PMMA (A) and PMMA-co-BM (B).

## 2.5 Research Objectives

2.2.1 To study the kinetic properties of  $\text{LiBH}_4$  nanoconfined in a PMMA-co-BM polymer matrix.

2.2.2 To study the interaction between PMMA-co-BM and  $\text{LiBH}_4$ .

2.2.3 To study the reaction mechanisms during de/rehydrogenation.

## 2.6 References

- Au, M., Jurgensen, A., and Zeigler, K. (2006). Modified lithium borohydrides for reversible hydrogen storage (2). **J. Phys. Chem. B.** 11: 26482-26487.
- Au, M., Spencer, W., Jurgensen, A., and Zeigler, C. (2008). Hydrogen storage properties of modified lithium borohydrides. **J. Alloys. Compd.** 462: 303-309.
- Bogdanovic, B., and Schwickardi, M. (1997). Ti-doped alkali metal aluminium hydrides as potential novel reversible hydrogen storage materials. **J. Alloys. Compd.** 253-254: 1-9.

- Bösenberg, U., Doppiu, S., Mosegaard, L., Barkhordariana, G., Eigena, N., and Borgschulte, A. (2007). Hydrogen sorption properties of MgH<sub>2</sub>-LiBH<sub>4</sub> composites. **Acta Mater.** 55: 3951-3958.
- Checchetto, R., Bazzanella, N., Miotello, A., Carotenuto, G., and Nicolais, L. (2009) Hydrogen sorption in metal-polymer composites: The role of interfaces. **J. Appl. Phys.** 105: 083513.
- Fu, Q. J., Ramirez-Cuesta, A. J., and Tsang, S. C. (2006). Molecular aluminum hydrides identified by inelastic neutron scattering during H<sub>2</sub> regeneration of catalyst-doped NaAlH<sub>4</sub>. **J. Phys. Chem. B.** 11: 711-715.
- Germain, J., Hradil, J., Frechet, J. M. J., and Svec, F. (2006). High surface area nanoporous polymers for reversible hydrogen storage. **Chem. Mater.** 18: 4430-4435.
- Gosalawit-Utke, R., Nielsen, T. K., Saldan, I. Laipple, D., Cerenius, Y., Jensen, T. R., Klassen, T., and Dornheim, M. (2011). Nanoconfined 2LiBH<sub>4</sub>-MgH<sub>2</sub> prepared by direct melt infiltration into nanoporous materials. **J. Phys. Chem. C.** 115: 10903-10910.
- Gross, A. F., Vajo, J. J., Van Atta, S. L., and Olson, G.L. (2008). Enhance hydrogen storage kinetics in nanoporous carbon scaffold. **J. Phys. Chem. C.** 112: 5651-5657.
- Guo, Y., Wu, H., Zhou, W., Yu, X. (2011). Dehydrogenation tuning of ammine borohydrides using double-metal cations. **J. Am. Chem. Soc.** 133: 4690-4693.
- Jeon, K. J., Moon, H. R., Ruminski, A. M., Jiang, B., Kisielowski, C., Bardhan, R., and Urban, J. J. (2011). Air-stable magnesium nanocomposites provide rapid And high-capacity hydrogen storage without using heavy-metal catalysts. **Nat.**

**Mater.** 10: 286-290.

Jurczyk, M. U., Kumara, A., Srinivasanb, S., and Stefanakosb, E. (2007). Polyaniline-based nanocomposite materials for hydrogen storage. **Int. J. Hydrogen Energ.** 32: 1010-1015.

Kang, X.D., Wang, P., Ma, L.P., and Cheng, H.M. (2007). Reversible hydrogen storage in  $\text{LiBH}_4$  destabilized by milling with Al. **Appl. Phys. A.** 89: 963-966.

Li, C., Peng, P., Zhou, D.W., and Wan, L. (2011). Research progress in  $\text{LiBH}_4$  for hydrogen storage: A review. **Int. J. Hydrogen Energ.** 36: 14512-14526.

Li, H.W., Orimo, S., Nakamori, Y., Miwa, K., Ohba, N., Towata, S., and Züttel, A. (2007). Materials designing of metal borohydrides: Viewpoints from thermodynamical stabilities. **J. Alloys. Compd.** 446-447: 315-318.

Liu, X., Peaslee, D., Jost, C. Z., Baumann, T. F., and Majzoub, E. H. (2011). Systematic pore-size effects of nanoconfinement of  $\text{LiBH}_4$ : elimination of diborane release and tunable behavior for hydrogen storage applications. **Chem. Mater.** 23: 1331-1336.

Mauron, P., Buchter, F., Friedrichs, O., Remhof, A., Biemann, M., Zwicky, C.N., and Züttel, A. (2008). Stability and reversibility of  $\text{LiBH}_4$ . **J. Phys. Chem. B.** 112: 906-910.

Nakamori, Y., Miwa, K., Ninomiya, A. Li, H., Ohba, N., Towata, S. (2006). Correlation between thermodynamical stabilities of metal borohydrides and cation electronegativities: First-principles calculations and experiments. **Phys. Rev. B.** 74: 045126-045134.

Ngene, P., Adelhelm, P., Andrew, M., Krijn P. de Jong, and Petra E. de Jongh. (2010).  $\text{LiBH}_4$ /SBA-15 nanocomposites prepared by Melt infiltration under hydrogen

- pressure: synthesis and hydrogen sorption properties. **J. Phys. Chem. C.** 114: 6163-6168.
- Nielsen, T. K., Bösenberg U., Gosalawit, R., Dornheim, M., Cerenius, Y., Besenbacher, F., and Jensen, T. R. (2010). A reversible nanoconfined chemical reaction. **ACS Nano.** 4(7): 3903-3908.
- Orimoa, S., Nakamoria, Y., Kitaharaa, G., Miwab, K., Ohbab, N., Towatab, S., and Züttelc, A. (2005). Dehydrodiding and rehydrodiding reactions of LiBH<sub>4</sub>. **J. Alloys. Compd.** 404-406: 427-430.
- Rongeata, C., Annac, V. D., Hagemannc, H., Borgschulteb, A., Züttelb, A., Schultza, L., and Gutfleischa, O. (2010). Effect of additives on the synthesis and reversibility of Ca(BH<sub>4</sub>)<sub>2</sub>. **J. Alloys. Compd.** 493: 281-287.
- Silvearv, F. (2011). **First principle studies of functional materials. Hydrogen storage and cutting tools.** (pp. 37-44). Sweden: Acta Universitatis Upsaliensis.
- Srinivasan, S. S., Ratnadurai, R., Niemann, M. U., Phan, A. R., Goswami, D. Y., and Stefanakos, E. K. (2010). Reversible hydrogen storage in electrospun polyaniline fibers. **Int. J. Hydrogen Energ.** 35: 225-230.
- Sun, D., Srinivasan, S. S., Kiyobayashi, T., Kuriyama, N., and Jensen, C. M. (2003). Rehydrogenation of dehydrogenated NaAlH<sub>4</sub> at low temperature and pressure. **J. Phys. Chem. B.** 17: 1176-10179.
- Sutton, A. D., Burrell, A. K., Dixon, D. A., Garner, E. B., Gordon, J. C., Nakagawa T., Ott, K. C., Robinson, J. P., and Vasiliu, M. (2011). Regeneration of ammonia borane spent fuel by direct reaction with hydrazine and liquid ammonia. **Science.** 331: 1426-1429.

- Vajo, J. J., and Olson, G. L. (2007). Hydrogen storage in destabilized chemical systems. **Scripta Mater.** 56: 829-834.
- Vajo, J. J., Salguero, T. T., Gross, A. F., Skeith, S. L., and Olson, G. L. (2007). Thermodynamic destabilization and reaction kinetics in light metal hydride systems. **J. Alloys. Compd.** 446-447: 409-414.
- Vajo, J. J., and Skeith, S. L. (2005). Reversible storage of hydrogen in destabilized  $\text{LiBH}_4$ . **J. Phys. Chem. B.** 19: 3719-3722.
- Xiong, Z., Yong, C. K., Wu, G., Chen, P., Shaw, W., Karkamkar, A. et al. (2007). High-capacity hydrogen storage in lithium and sodium amidoboranes. **Nat. Mater.** 7: 138-141.
- Yang, J., Sudik, A., and Wolverton, C. (2007). Destabilizing  $\text{LiBH}_4$  with a Metal (M = Mg, Al, Ti, V, Cr, or Sc) or Metal Hydride ( $\text{MH}_2 = \text{MgH}_2, \text{TiH}_2, \text{or CaH}_2$ ). **J. Phys. Chem. C.** 111: 19134-19140.
- Zhang, Y., Zhang, W. S., Wang, A. Q., Suna, L. X., Fana, Me. Q., Chua, H. L. et al. (2007).  $\text{LiBH}_4$  nanoparticles supported by disordered mesoporous carbon: Hydrogen storage performances and destabilization mechanisms. **Int. J. Hydrogen Energ.** 32: 3976-3980.
- Züttel, A., Wenger, P., Rentsch, S., Sudan, P., Mauron, Ph., and Emmenegger, Ch. (2003).  $\text{LiBH}_4$  a new hydrogen storage material. **J. Power Sources.** 118: 1-7.



## CHAPTER III

### EXPERIMENT

#### 3.1 Sample Preparation

##### 3.1.1 Purification of tetrahydrofuran

Tetrahydrofuran (THF) (HPLC grade, QRëC™) 500.00 ml were pre-dried by molecular sieves at room temperature for 24 h. Na (5.0014 g) and benzophenone (20.0006 g) were added into the pre-dried THF and the mixture was refluxed under nitrogen atmosphere at 80 °C for 24 h until the color of the solvent was changed to blue color. The mixture was distilled in nitrogen atmosphere at 70 °C to obtain purified THF (Schwartz, 1978).

##### 3.1.2 Precipitation of poly (methyl methacrylate)-co-butyl methacrylate

To remove the additives in the commercial polymer, poly (methyl methacrylate)-co-butyl methacrylate (PMMA-co-BM) ( $M_w = 75,000$ , Sigma Aldrich) of 20.4893 g were dissolved in 100.00 ml tetrahydrofuran (THF) (HPLC grade, QRëC™) to produce homogeneous PMMA-co-BM solution (20.0 % w/v). PMMA-co-BM solution was precipitated in n-hexane (AR grade, QRëC™) and dried at 90 °C for 24 h in an oven.

##### 3.1.3 Synthesis of nanoconfined $\text{LiBH}_4$ in poly (methyl methacrylate)-co-butyl methacrylate (PMMA-co-BM)



Precipitated poly (methyl methacrylate)-co-butyl methacrylate (PMMA-co-BM) of 5.0656 g was dissolved in 20.00 ml purified THF (prepared in 3.1.1) to produce homogeneous PMMA-co-BM solution (25.0 % w/v). 15.00 ml of lithium borohydride ( $\text{LiBH}_4$ ) (2 M in THF, Sigma Aldrich) were added to the PMMA-co-BM solution. The mixture was stirred overnight at room temperature under an argon atmosphere in a glove box. A transparent gel of  $\text{LiBH}_4$  nanoconfined in PMMA-co-BM was obtained. The sample was dried in the glove box at room temperature for several days. The dried gel, denoted as nanoconfined  $\text{LiBH}_4$ -PMMA-co-BM was ground in the mortar to obtain the fine powder.

#### 3.1.4 Preparation of milled $\text{LiBH}_4$

The powder sample of  $\text{LiBH}_4$  0.6397 g ( $\geq 90\%$  hydrogen-storage grade, Sigma Aldrich) was milled by using a SPEX CertiPrep 8000D DUAL Mixer/Mill under a nitrogen atmosphere. Ball-to-powder weight ratio (BPR) and milling time were 10:1 and 5 h, respectively.

### 3.2 Characterizations

#### 3.2.1 Powder X-ray diffraction (XRD) measurements

Powder X-ray diffraction (XRD) was carried out on the powder samples of PMMA and nanoconfined  $\text{LiBH}_4$ -PMMA-co-BM by using a Bruker axis D5005,  $\text{CuK}_\alpha$  ( $\lambda = 1.5406 \text{ \AA}$ ) radiation. The sample of approximately 7-10 g was packed in a sample holder before exposure to X-ray beam. All XRD experiments were conducted at room temperature. The scanning step was  $0.02^\circ/\text{s}$ . The scanning  $2\theta$  was in the range of  $10-80^\circ$ .

### 3.2.2 Scanning electron microscopy (SEM)

The powder sample of nanoconfined  $\text{LiBH}_4\text{-PMMA-co-BM}$  was deposited onto the sample holder by using silver glue (in *n*-butyl acetate). The sample was coated by platinum (Pt) sputtering with the current of 30 mA for 30 s under vacuum. The sample was loaded into a scanning electron microscope (SEM), performed by using an Auriga from Zeiss, Germany. An energy-dispersive X-ray spectroscopy (EDS)-mapping was carried out by an apparatus from EDAX Inc., USA. Smart SEM and EDS Genesis programs were used for morphology studied and elemental investigation, respectively.

### 3.2.3 Coupled manometric-calorimetric measurements

Coupled manometric-calorimetric measurements of nanoconfined  $\text{LiBH}_4\text{-PMMA-co-BM}$  and milled  $\text{LiBH}_4$  were carried out by connecting a Sievert-type apparatus (a PCTPro-2000, Setaram & Hy-Energy) with a high-pressure calorimeter (a Sensys DSC, Setaram). A high-pressure cell of the calorimeter, connected to the manometric instrument by a 1/8 inch stainless steel tube was loaded with ~ 13–25 mg of the powder samples in the glove box. Dehydrogenation was performed by heating the samples from room temperature to 300 °C (nanoconfined  $\text{LiBH}_4\text{-PMMA-co-BM}$ ) and to 600 °C (milled  $\text{LiBH}_4$ ) with the heating rate of 5 °C/min under vacuum. The calorimetric profiles were analyzed by a Calisto software to achieve the peaks temperature.

### 3.2.4 Gas analysis

The analysis of gases evolved upon dehydrogenation of nanoconfined

LiBH<sub>4</sub>-PMMA-co-BM sample was performed by connecting the manometric PCTPro-2000 apparatus with a residual gas analyzer RGA200 (Setaram, France) by using a 1/8 inch stainless steel tube. The powder sample of ~200 mg was loaded in the sample holder and assembled to the PCTPro-2000 apparatus. The sample was heated from room temperature to 300 °C at 5 °C/min under vacuum. The signal of the gases released from the sample was continuously recorded.

### 3.2.5 Kinetic measurements

Kinetic properties of nanoconfined LiBH<sub>4</sub>-PMMA-co-BM, milled LiBH<sub>4</sub>, and PMMA-co-BM were studied and compared by using a laboratory scale setup of a Sievert-type apparatus (Figure 3.1). The powder samples (100-200 mg) was packed in a high pressure stainless steel sample holder (316SS, Swagelok) under argon atmosphere of the glove box and transferred to the Sievert-type apparatus. Two K-type thermocouples (-250–1,300 °C, SL heater) were attached to the sample holder and the furnace to measure the temperature of the system. Pressure transducers (C206, Cole Parmer) in the pressure range of 0-100 psig and 0-3000 psig were used to measure the pressure change due to hydrogen desorption and absorption, respectively. Thermocouples and pressure transducers were connected to an AI 210I module convertor data logger (Wisco), measuring and transferring (every 1 s) the pressure and temperature changes of the sample to the computer for further evaluation. Dehydrogenation of nanoconfined LiBH<sub>4</sub>-PMMA was done by heating the sample to 120 °C (vacuum) via a furnace controlled by a PID temperature controller. In the case of rehydrogenation, the powder sample was pressurized under hydrogen (purity= 99.999 %) pressure of 50 bar at 140 °C for 12 h. Once the pressure reading was

constant over a period of time, the amount of hydrogen release and uptake was calculated by the pressure change ( $\Delta P$ ) using the following equations:

$$(\Delta P)V = nRT$$

$$H_2 \text{ desorbed (wt. \%)} = [(n \times 2.0158) / \text{sample weight}] \times 100$$

where  $P$ ,  $V$ , and  $T$  are hydrogen pressure (atm), volume of the system (L), and temperature (K), respectively,  $n$  is the number of hydrogen moles (mol), and  $R$  is gas constant ( $0.0821 \text{ L atm K}^{-1} \text{ mol}^{-1}$ ).

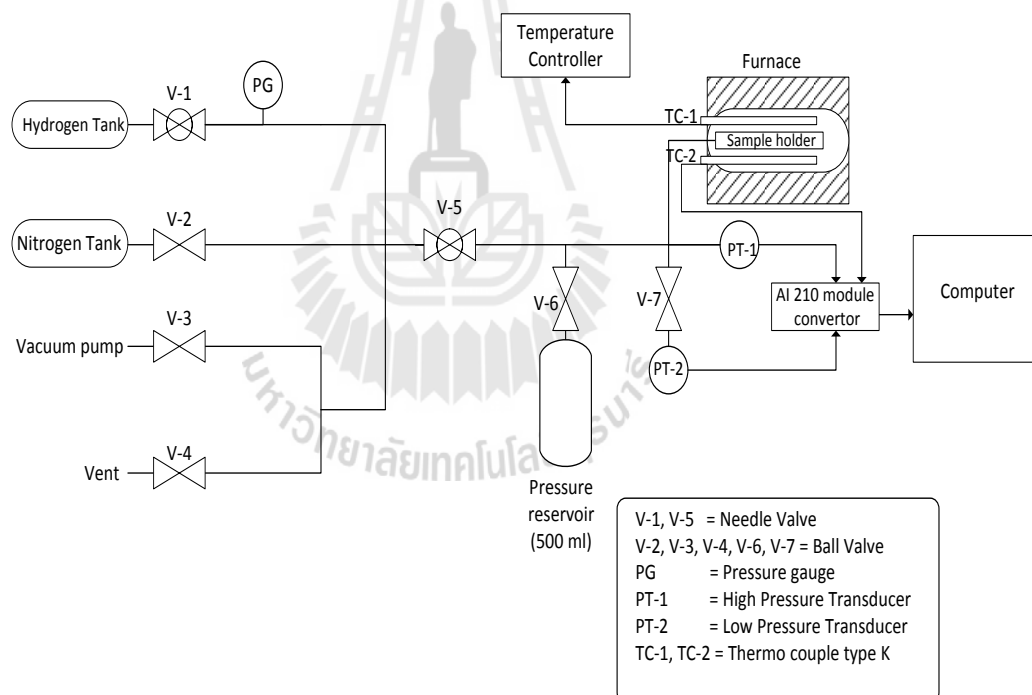


**Figure 3.1** Schematic diagram of Sievert-type apparatus.

### 3.2.6 Fourier transform infrared spectroscopy (FTIR)

The powder samples of milled  $\text{LiBH}_4$ , PMMA-co-BM, and the

nanoconfined  $\text{LiBH}_4\text{-PMMA-co-BM}$  were investigated by Fourier Transform Infrared Spectrophotometer (FT-IR) using a Spectrum GX, Perkin Elmer. The mixture of sample powder and anhydrous KBr was ground in the mortar with the weight ratio of  $\sim 1:10$  (sample powder: KBr), and pressed under a specific pressure into a pellet of 1 cm diameter. The KBr pellet containing the sample was assembled in the instrument, where it was on the infrared direction. The spectra were collected in the wavenumber range of  $4000\text{-}450\text{ cm}^{-1}$  with 32 scans for both sample and background. To accomplish the final spectrum, subtraction of the sample spectrum with that of the background was done.

### 3.2.7 Nuclear magnetic resonance (NMR) measurement

Solid-State  $^{11}\text{B}$  and  $^{13}\text{C}$  magic angle spinning nuclear magnetic resonance (MAS NMR) spectra were recorded by a Bruker ASCEND<sup>TM</sup> 500 using CPMAS BL4 VTN probe. The NMR measurements were performed at 302 K and the samples were tightly packed in a zirconia end-capped tube. The  $^{11}\text{B}$  and  $^{13}\text{C}$  chemical shifts were detected in part per million (ppm) relative to neat boric acid ( $\text{H}_2\text{BO}_3$ ) and tetramethylsilane ( $\text{Si}(\text{CH}_3)_4$ ), respectively. A spinning speed ( $\nu_R$ ) of 10 kHz and 1,000 scans were carried out.

### 3.2.8 X-ray photoelectron spectroscopy (XPS)

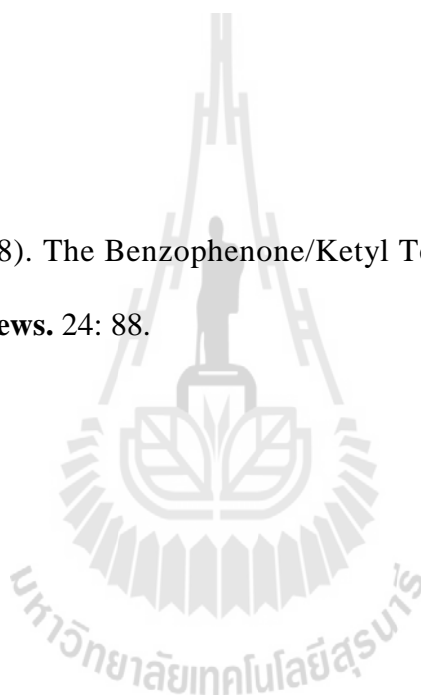
X-ray photoelectron spectroscopy (XPS) was carried out at the Siam Photon Laboratory, BL3.2a in the Synchrotron Light Research Institute, Nakhon Ratchasima, Thailand. The powder samples of milled  $\text{LiBH}_4$  and nanoconfined  $\text{LiBH}_4\text{-PMMA-co-BM}$  at different states of before desorption, after desorption, and

after absorption were held on the sample holders by using carbon glue tape in the glove box atmosphere. Prior to the measurements, all prepared samples were placed in an ultrahigh vacuum chamber for approximately 6 h. A photon energy of 400 eV was used to detect the signals of Li 1s and B 1s. Each element was investigated at the kinetic energy step of 0.1 eV for 5 scans by using an CLAM2 analyzer. The multi spectra were analyzed by using a macro XPS MS Excel 2007 (Windows XP) software.

### 3.3 Reference

Schwartz, A.M. (1978). The Benzophenone/Ketyl Tetrahydrofuran (THF) Still.

**Chem. Eng. News.** 24: 88.





# CHAPTER IV

## RESULTS AND DISCUSSION

### 4.1 Results and Discussion

#### 4.1.1 Nanoconfinement of $\text{LiBH}_4$ in PMMA-co-BM polymer matrix

To investigate the nanoconfinement of the  $\text{LiBH}_4$  nanoparticles in PMMA-co-BM matrix, powder X-ray diffraction (XRD) measurement was used. Figure 4.1 (a) shows a broad peak at  $2\theta = 14^\circ$ , according to the amorphous nature of PMMA as well as two broad peaks at  $2\theta$  of  $29.7^\circ$  and  $41.7^\circ$ , respectively (Motaung et al., 2012). In the case of nanoconfined  $\text{LiBH}_4$ -PMMA-co-BM (Figure 4.1 (b)), peak shows up approximately at the same  $2\theta$  as for PMMA (Figure 4.1 (a)), however, broader peaks and lower intensity are observed. This suggests a higher amorphous degree of PMMA-co-BM, which results from the nanoconfinement of  $\text{LiBH}_4$  in between PMMA-co-BM polymer chains. Moreover, the nanoconfinement of  $\text{LiBH}_4$  in PMMA-co-BM polymer matrix was also confirmed by SEM and EDS-mapping (Figure 4.2).



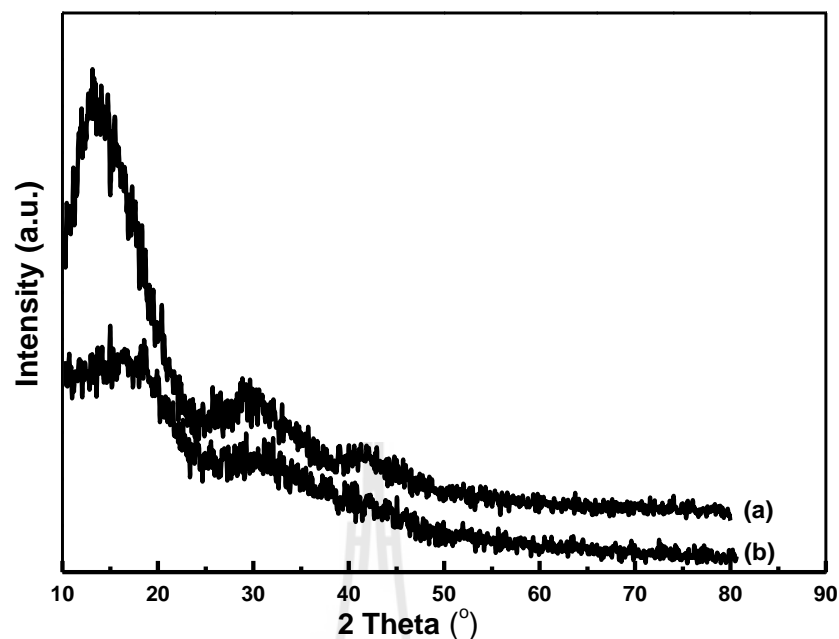


**Figure 4.1** XRD patterns of PMMA-co-BM (a) and nanoconfined LiBH<sub>4</sub>-PMMA-co-BM (b).

In the case of SEM and EDS-mapping, Figure 4.2 (A) shows the surface morphology of nanoconfined LiBH<sub>4</sub>-PMMA-co-BM, where EDS-mapping analysis was detected. Figures 4.2 (B) and (C) exhibit good dispersion of carbon (C) and oxygen (O) atoms (PMMA-co-BM), respectively. In the case of boron (B), representing LiBH<sub>4</sub> homogeneous dispersion all over PMMA-co-BM polymer matrix is observed (Figure 4.2 (D)). Figure 4.2 (E) shows the amount of (1) oxygen (O) (2) carbon (C) from PMMA-co-BM structure and oxygen in atmosphere, (3) boron (B) from LiBH<sub>4</sub> and (4) platinum (Pt) from surface coating on sample, respectively. On the basis of EDS technique, it is not sensitive to light elements, the signal of lithium (Li) atoms from LiBH<sub>4</sub> cannot be detected.

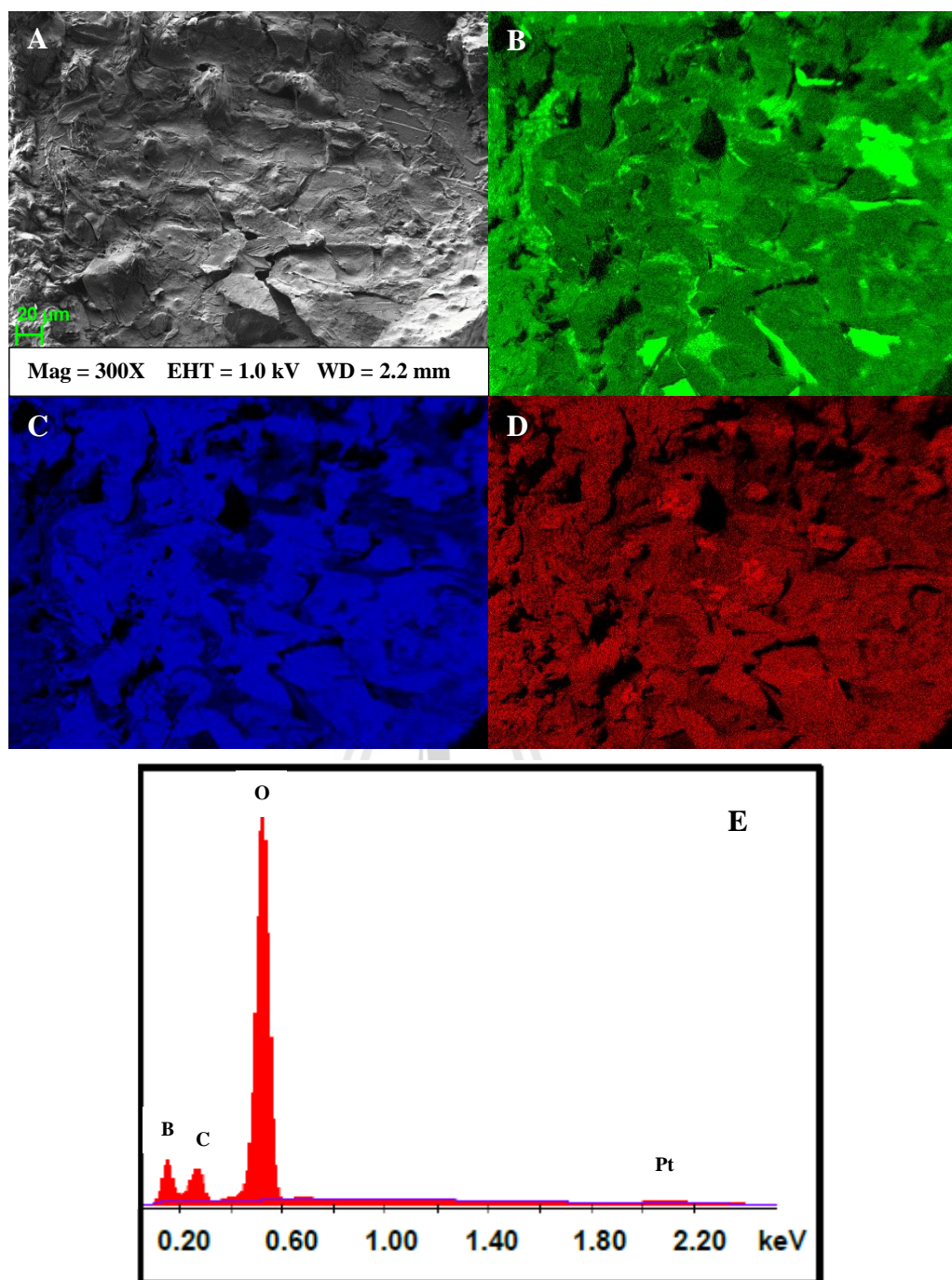


**Figure 4.2** SEM image of nanoconfined  $\text{LiBH}_4$ -PMMA-co-BM (A), carbon mapping (B), oxygen mapping (C), boron mapping (D), and quantitative elemental analysis (E).

#### 4.1.2 Dehydrogenation profiles

To prove that the experimental data is reliable, comparison with the theoretical values is required. The theoretical hydrogen storage capacities of samples calculated from the amount of all components in the mixtures are shown in Table 4.1. Nanoconfined LiBH<sub>4</sub>-PMMA-co-BM contains 11.53 wt.% of LiBH<sub>4</sub>. On the basis of the milled LiBH<sub>4</sub>, 13.8 wt.% H<sub>2</sub> is obtained as a theoretical storage capacity calculated from the following equation (Li et al., 2011):



Therefore, the theoretical hydrogen storage capacity of the nanoconfined LiBH<sub>4</sub>-PMMA-co-BM is 1.59 wt.% (Table 4.1).

**Table 4.1** Amount of components and theoretical and experimental hydrogen storage capacities of milled and nanoconfined samples.

Sample	Amount (g)		LiBH <sub>4</sub> Content (wt.%)	Theoretical H <sub>2</sub> storage capacity (wt.% H <sub>2</sub> )	H <sub>2</sub> storage capacity (1 <sup>st</sup> desorption) (wt.% H <sub>2</sub> )
	LiBH <sub>4</sub>	PMMA			
1)Milled LiBH <sub>4</sub>	0.6397	-	100.0	13.80	0.00
2)LiBH <sub>4</sub> -PMMA-co-BM	0.6600	5.0656	11.53	1.59	0.78

Coupled manometric-calorimetric analysis under 5 °C/min heating rate was performed to characterize the dehydrogenation profiles of milled LiBH<sub>4</sub> (room temperature to 600 °C) and nanoconfined LiBH<sub>4</sub>-PMMA-co-BM samples (room temperature to 300 °C). Figure 4.3 shows the endothermic peaks of o-LiBH<sub>4</sub> to h-LiBH<sub>4</sub> phase transformation and h-LiBH<sub>4</sub> melting of milled LiBH<sub>4</sub> at 119 and 287

°C, respectively. By heating the sample up to 482 °C, an endothermic peak of  $\text{LiBH}_4$  dehydrogenation is observed. From the manometric profiles, milled  $\text{LiBH}_4$  starts to release hydrogen at  $\sim 290$  °C and reveal 6.3 wt. %  $\text{H}_2$  released (45.65 % of theoretical hydrogen storage capacity) at temperature up to 550 °C (Figure 4.3). For comparison, the coupled manometric–calorimetric analysis was also performed on nanoconfined  $\text{LiBH}_4$ –PMMA–co–BM sample (Figure 4.4).

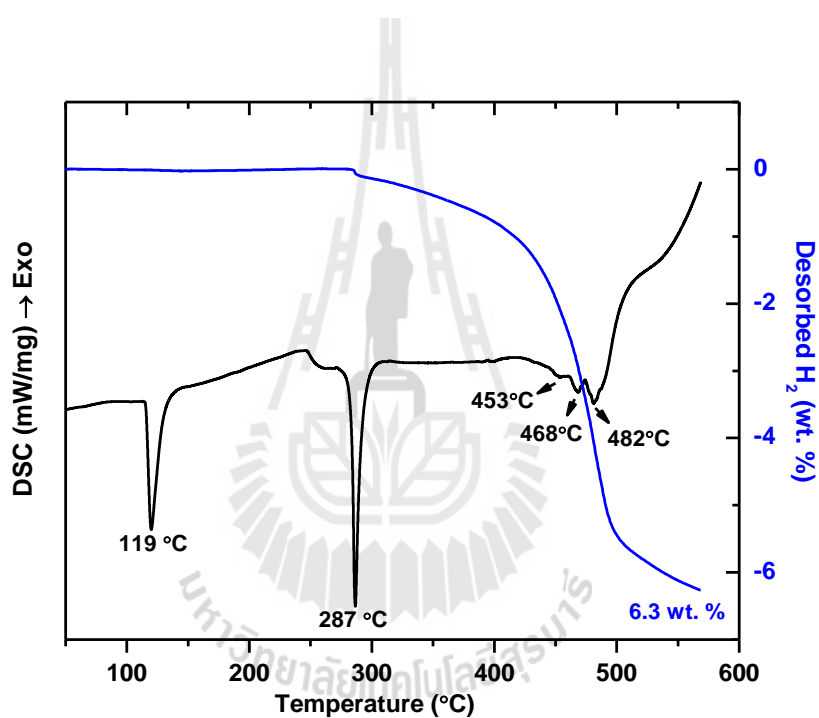


**Figure 4.3** Dehydrogenation profiles and hydrogen storage capacity of milled  $\text{LiBH}_4$ .

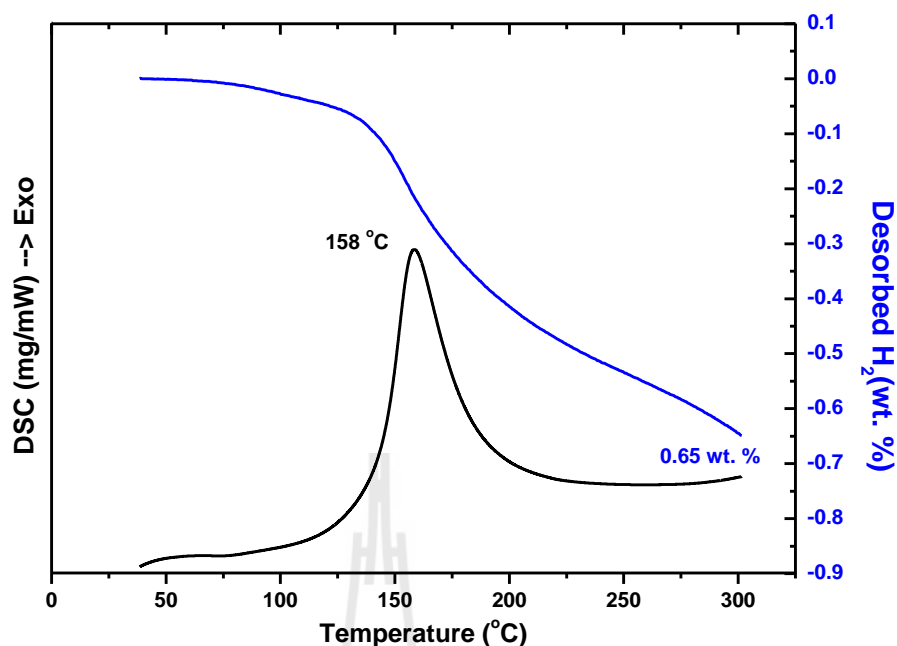


**Figure 4.4** Dehydrogenation profiles from coupled manometric-calorimetric analysis of nanoconfined LiBH<sub>4</sub>-PMMA-co-BM.

From Figure 4.4, nanoconfined LiBH<sub>4</sub>-PMMA-co-BM shows an exothermic peak at 158 °C, corresponding to the dehydrogenation of LiBH<sub>4</sub>, the mechanism is further discussed in section 4.1.4 (interaction between LiBH<sub>4</sub> and PMMA-co-BM). In the case of H<sub>2</sub> desorption, the sample releases 0.65 wt.% of H<sub>2</sub> in the temperature range of room temperature to 300 °C (Figure 4.4). From the manometric profiles, it should be mentioned that the dehydrogenation temperature of nanoconfined LiBH<sub>4</sub>-PMMA-co-BM is shifted significantly to lower temperature as compared to the milled LiBH<sub>4</sub>; that is,  $\Delta T = 324$  °C for dehydrogenation. Furthermore, it should be noted that phase transformation and melting of LiBH<sub>4</sub> in nanoconfined LiBH<sub>4</sub>-PMMA-co-BM disappear, suggesting the amorphous state of LiBH<sub>4</sub> due to completely nanoconfined in PMMA-co-BM polymer matrix.

Nevertheless, it cannot be concluded that nanoconfined  $\text{LiBH}_4$ -PMMA-co-BM desorbs only hydrogen because PMMA-co-BM may be degraded or deformed during dehydrogenation at high temperature. Therefore, gas analysis was performed to determine the gas species released during decomposition of nanoconfined  $\text{LiBH}_4$ -PMMA-co-BM (Figure 4.5).

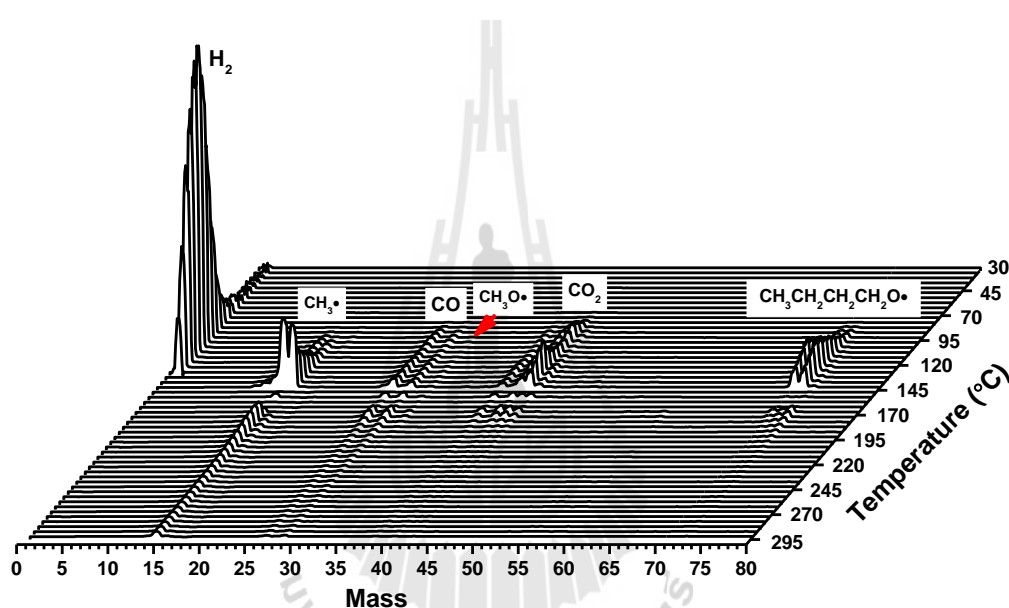


**Figure 4.5** Gas analysis during dehydrogenation of nanoconfined  $\text{LiBH}_4$ -PMMA-co-BM.

From Figure 4.5, it can be confirmed that the main gas product released from nanoconfined  $\text{LiBH}_4$ -PMMA-co-BM in the temperature range of 30–300 °C is hydrogen ( $\text{H}_2$ ) together with carbon monoxide ( $\text{CO}$ ), carbon dioxide ( $\text{CO}_2$ ), methyl radical ( $\text{CH}_3\bullet$ ), methoxy radical ( $\text{CH}_3\text{O}\bullet$ ), and butoxy radical ( $\text{CH}_3\text{CH}_2\text{CH}_2\text{CH}_2\text{O}\bullet$ ). It was reported that carbon monoxide ( $\text{CO}$ ), carbon dioxide ( $\text{CO}_2$ ), methyl ( $\text{CH}_3\bullet$ ), methoxy radicals ( $\text{CH}_3\text{O}\bullet$ ), are due to thermal degradation of PMMA (Kashiwagi and

Inabi, 1989; Rajkumar et al., 2010; Chang et al., 2001). Moreover, the butoxy radical ( $\text{CH}_3\text{CH}_2\text{CH}_2\text{CH}_2\text{O}\cdot$ ) due to thermal degradation of PMMA-co-BM was observed. Therefore, it can be concluded that not only dehydrogenation occurred in the temperature range of 30–300 °C, but also partial thermal degradation of the PMMA-co-BM polymer matrix. However, it should be noted that the amount of hydrogen is higher than others gases released from nanoconfined  $\text{LiBH}_4$ -PMMA-co-BM. From Figure 4.5, the onset and main desorption temperature of nanoconfined  $\text{LiBH}_4$ -PMMA-co-BM (80 and 105 °C, respectively) are lower than those of milled  $\text{LiBH}_4$  (290 and more than 450 °C, respectively (Figure 4.3)) and nanoconfined  $\text{LiBH}_4$  in 13 and 25 nm carbon aerogel (250 and 380 °C, respectively) ( $\Delta T = 210$  and  $170$  °C as compared with milled  $\text{LiBH}_4$  and nanoconfined  $\text{LiBH}_4$  in carbon aerogel, respectively) (Gross et al., 2008). This suggests the destabilization of  $\text{LiBH}_4$  after nanoconfinement in PMMA-co-BM polymer matrix. This significant improvement can be due to not only high surface area of  $\text{LiBH}_4$  nanoconfined in PMMA-co-BM polymer matrix, but also high hydrogen permeable property of PMMA-co-BM as well as interaction between  $\text{LiBH}_4$  and PMMA-co-BM, further discussed in section 4.1.4 (interaction between  $\text{LiBH}_4$  and PMMA-co-BM) and 4.1.6 (reaction mechanisms, and reversibility).

### 4.1.3 Dehydrogenation kinetics and reversibility

To evaluate the dehydrogenation kinetics, two hydrogen release and uptake cycles of nanoconfined  $\text{LiBH}_4$ -PMMA-co-BM and milled  $\text{LiBH}_4$  as well as gas desorption of PMMA-co-BM were carried out by titration measurements. Dehydrogenation and rehydrogenation were carried out at 120 °C (vacuum) and 140 °C

(50 bar H<sub>2</sub>), respectively.

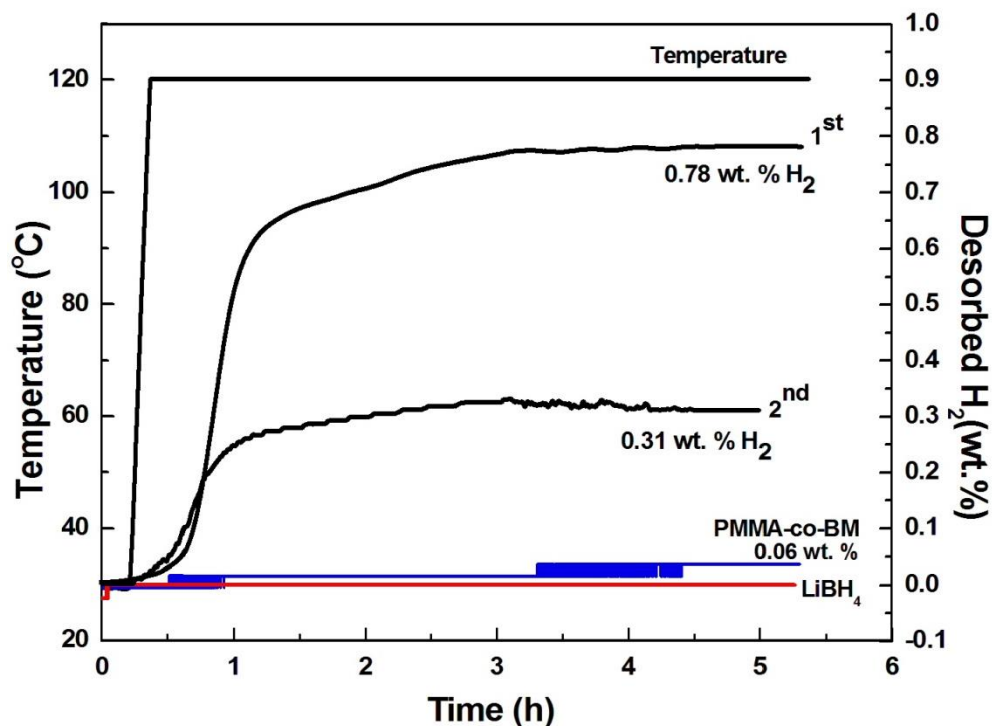


**Figure 4.6** Dehydrogenation kinetics of nanoconfined LiBH<sub>4</sub>-PMMA-co-BM, milled LiBH<sub>4</sub>, and PMMA-co-BM at 120 °C.

From Figure 4.6, after subtraction with amount of gas released from partial thermal degradation of PMMA-co-BM (~ 0.06 wt.%), nanoconfined LiBH<sub>4</sub>-PMMA-co-BM releases 0.78 wt.% H<sub>2</sub> within 2 h 30 min during the 1<sup>st</sup> cycle (5.96 wt.% H<sub>2</sub> with respect to LiBH<sub>4</sub> content). Thereafter, rehydrogenation was done at 140 °C under 50 bar H<sub>2</sub> for 12 h. It results in desorbed hydrogen of 0.31 wt.% H<sub>2</sub> (2.37 wt.% H<sub>2</sub> with respect to LiBH<sub>4</sub> content) during the 2<sup>nd</sup> dehydrogenation. This reveals almost 50% reversibility of nanoconfined LiBH<sub>4</sub>-PMMA-co-BM. With respect to the second hydrogen desorption capacity, it should be due to the partial thermal



degradation of PMMA-co-BM during the first desorption/absorption (Figure 4.5). This probably leads to unstable nanoconfinement of LiBH<sub>4</sub> in PMMA-co-BM polymer matrix. Therefore, the temperature, pressure, and time for rehydrogenation may not be enough to absorb hydrogen completely. In the case of inferior amount of H<sub>2</sub> released during 1<sup>st</sup> dehydrogenation (0.78 wt.% H<sub>2</sub>) with respect to theoretical value (1.59 wt.% H<sub>2</sub>) it might be due to the interaction between LiBH<sub>4</sub> and PMMA-co-BM polymer chains, discussed in section 4.1.4 (interaction between LiBH<sub>4</sub> and PMMA-co-BM) and 4.1.6 (reaction mechanisms and reversibility). However, with respect to the 1<sup>st</sup> and 2<sup>nd</sup> desorption, nanoconfined LiBH<sub>4</sub>-PMMA-co-BM give remarkably superior desorption kinetics than the milled LiBH<sub>4</sub> (no H<sub>2</sub> release). For example, more than 400 °C is required for total dehydrogenation of milled material during the 1<sup>st</sup> cycle (Blanchard et al., 2009), whereas the nanoconfined sample needs below 120 °C. This suggests a significant improvement of desorption/absorption conditions in nanoconfined LiBH<sub>4</sub>-PMMA-co-BM as compared to the milled material.

#### 4.1.4 Interaction between LiBH<sub>4</sub> and PMMA-co-BM

To determine the reaction mechanisms during de/rehydrogenation and interaction between LiBH<sub>4</sub> and PMMA-co-BM polymer matrix, FTIR, solid-state <sup>13</sup>C and <sup>11</sup>B MAS NMR techniques were performed. From Figure 4.7 (a), LiBH<sub>4</sub> reveals the characteristic peaks of B-H vibrations at 2388, 2290, 2227, and 1127 cm<sup>-1</sup>. The peak at 1638 cm<sup>-1</sup> refers to O-H bond, which should be due to air and moisture contamination during the experiment. For PMMA-co-BM, Figure 4.7 (b) shows vibrational peak corresponding to C=O stretching of ester group at 1730 cm<sup>-1</sup>. The

two doublet bands at 1271-1242 and 1192-1153  $\text{cm}^{-1}$  are C–O stretching vibrations of ester group. The peaks around 1452 and 1485  $\text{cm}^{-1}$  belong to asymmetric bending vibrations of (C–CH<sub>3</sub>) and (C–CH<sub>2</sub>) bonds, respectively (Namouchi et al., 2009). After nanoconfinement of LiBH<sub>4</sub> in PMMA-co-BM, Figure 4.7 (c) exhibits all characteristic peaks of both LiBH<sub>4</sub> and PMMA-co-BM, indicating that LiBH<sub>4</sub> was successfully embedded in PMMA-co-BM. Moreover, the characteristic peak of B–O bond is observed at 1384  $\text{cm}^{-1}$  (Mohlala and Strydom, 2009). A shoulder at 1707  $\text{cm}^{-1}$  suggests that the local environment of carbonyl group (C=O) in PMMA-co-BM structure changes upon embedding with LiBH<sub>4</sub>. With respect to metal ion–carbonyl interaction, the vibrational peak of carbonyl group is shifted to lower wavenumber as previously reported (Lim et al., 2008), corresponding to an interaction between boron atoms (B) of LiBH<sub>4</sub> and PMMA-co-BM at oxygen atoms (O) (–OCH<sub>3</sub> or –OCH<sub>2</sub>CH<sub>2</sub>CH<sub>2</sub>CH<sub>3</sub>) and interaction of carbonyl groups (from PMMA-co-BM) with Li<sup>+</sup> ions (from LiBH<sub>4</sub> in THF solution).

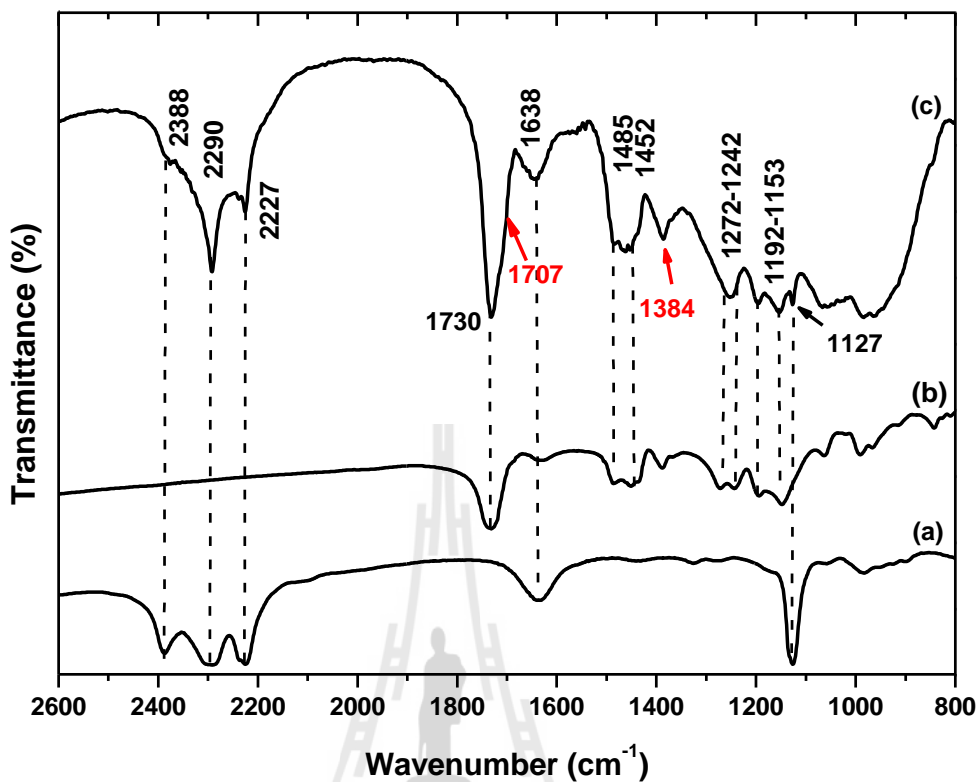


**Figure 4.7** FTIR spectra of LiBH<sub>4</sub> (a), PMMA-co-BM (b), and nanoconfined LiBH<sub>4</sub>-PMMA-co-BM (c).

Moreover, solid state <sup>13</sup>C NMR was performed to study the interaction between LiBH<sub>4</sub> and PMMA-co-BM polymer chains (Figure 4.8 and 4.9).

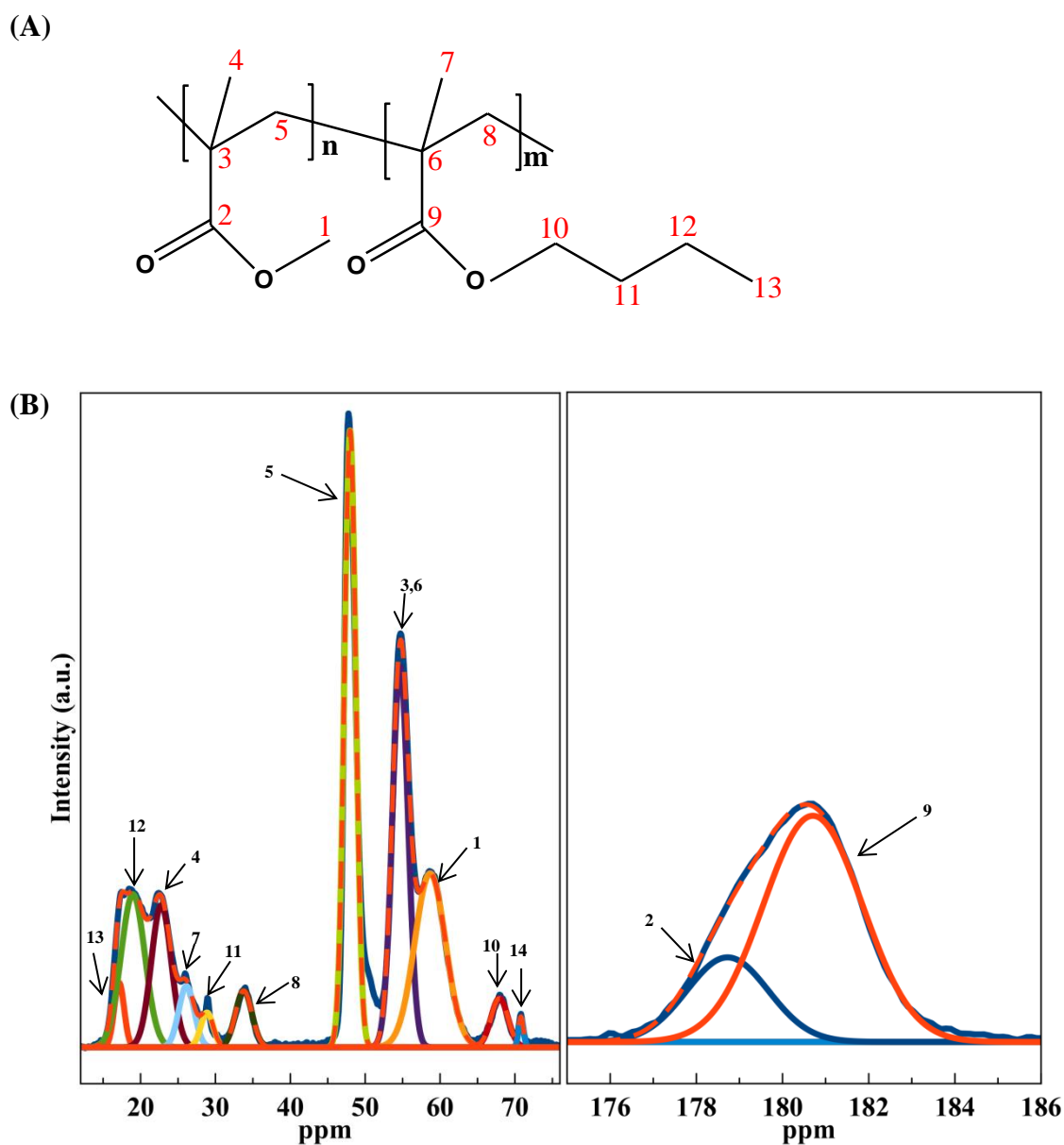


**Figure 4.8** Chemical structure (A) and  $^{13}\text{C}$  NMR (B) of PMMA-co-BM.

In Figure 4.8 (B), peaks at 17–48 ppm (4-5, 7-8, and 11-13) are corresponding to methyl and methylene groups ( $-\text{CH}_3$  and  $-\text{CH}_2$ ) of PMMA-co-BM, as well as peaks 3 and 6 at 54.67 ppm relate to quaternary carbon of PMMA-co-BM structure. Peaks 1, 10, and 14 (58.67, 67.93, and 70.82 ppm, respectively) refer to methoxy ( $-\text{OCH}_3$ ), butoxy ( $-\text{OCH}_2\text{CH}_2\text{CH}_2\text{CH}_3$ ) groups, and ether bond of THF

( $-\text{CH}_2-\text{O}-\text{CH}_2$ ), respectively. Peaks 2 and 9 (178.72 and 180.70 ppm, respectively) are carbonyl carbon ( $\text{C}=\text{O}$ ) of methoxy and butoxy positions, respectively.

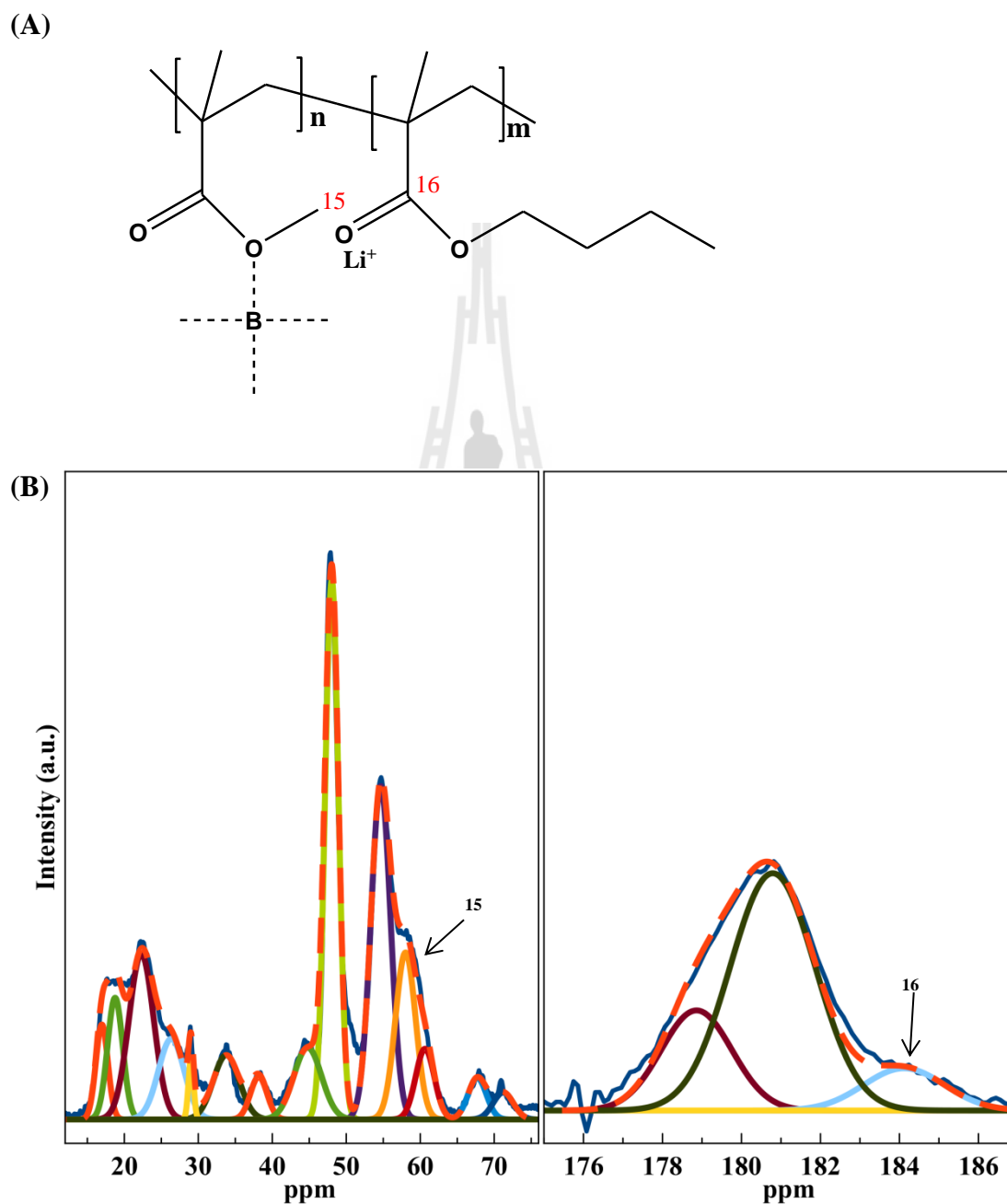


**Figure 4.9** Chemical structure (A) and  $^{13}\text{C}$  NMR (B) of nanoconfined  $\text{LiBH}_4$ -PMMA-co-BM (B).

After nanoconfinement of  $\text{LiBH}_4$  into PMMA-co-BM polymer matrix, Figure 4.9 (B) reveals all peaks similar to PMMA-co-BM (Figure 4.8 (B)) together with the additional responds of peaks 15 and 16 at 58.01 and 184.11 ppm, respectively. On the basis of NMR measurement, a nucleus of interest carbon atom is shielded by electron cloud. Electrons under the influence of magnetic field circulate and create their own magnetic field interrupting the applied field, called "shielding" effect. On the other hand, element with high electronegativity attached to carbon atom resulting in the reduction of electron density around this carbon atoms, called "deshielding" effect. The higher the shielding effect, the lower the chemical shift. At peak 15 at 58.01 ppm, this could be due to the more electron density around methoxyl ( $-\text{OCH}_3$ ) group due to the interaction between boron atoms (B) and borohydride molecules ( $\text{BH}_4^-$ ) of  $\text{LiBH}_4$  with  $-\text{OCH}_3$  group, which is less electronegativity than oxygen atoms (O). This result relates to B-O bond in FTIR measurement (Figure 4.7 (c)). In the case of peak 16 at 184.11 ppm, it corresponds to deshielding of C=O group via interaction with electronegative groups or in this case  $\text{Li}^+$  ion, in accordance with a shoulder at  $1707\text{ cm}^{-1}$  in FTIR spectra (Figure 4.7 (c)). Thereby, FTIR and  $^{13}\text{C}$  NMR spectra conclude the interaction between  $\text{LiBH}_4$  and PMMA-co-BM polymer chains at  $-\text{OCH}_3$  with borohydride ( $\text{H}_{(4-x)}\text{B}---(\text{OCH}_3)_x$ ), boron atoms ( $\text{B}---(\text{OCH}_3)_4$ ), and at C=O ( $\text{Li}^+---\text{O}=\text{C}$ ) positions (Figure 4.10 (A) and (B)). The formations of ( $\text{H}_{(4-x)}\text{B}---(\text{OCH}_3)_x$ ) and ( $\text{B}---(\text{OCH}_3)_4$ ) may be due to the cross linking of PMMA-co-BM by  $\text{LiBH}_4$ , as shown in the gel formation after mixing PMMA-co-BM with  $\text{LiBH}_4$ . With respect to the interaction formations of ( $\text{H}_{(4-x)}\text{B}---(\text{OCH}_3)_x$ ) and ( $\text{B}---(\text{OCH}_3)_4$ ) in nanoconfined  $\text{LiBH}_4$ -PMMA-co-BM, it exhibits the partial desorption of  $\text{LiBH}_4$  during sample preparation, resulting in amount of hydrogen released less than the theoretical

capacity from coupled manometric–calorimetric and titration measurements.

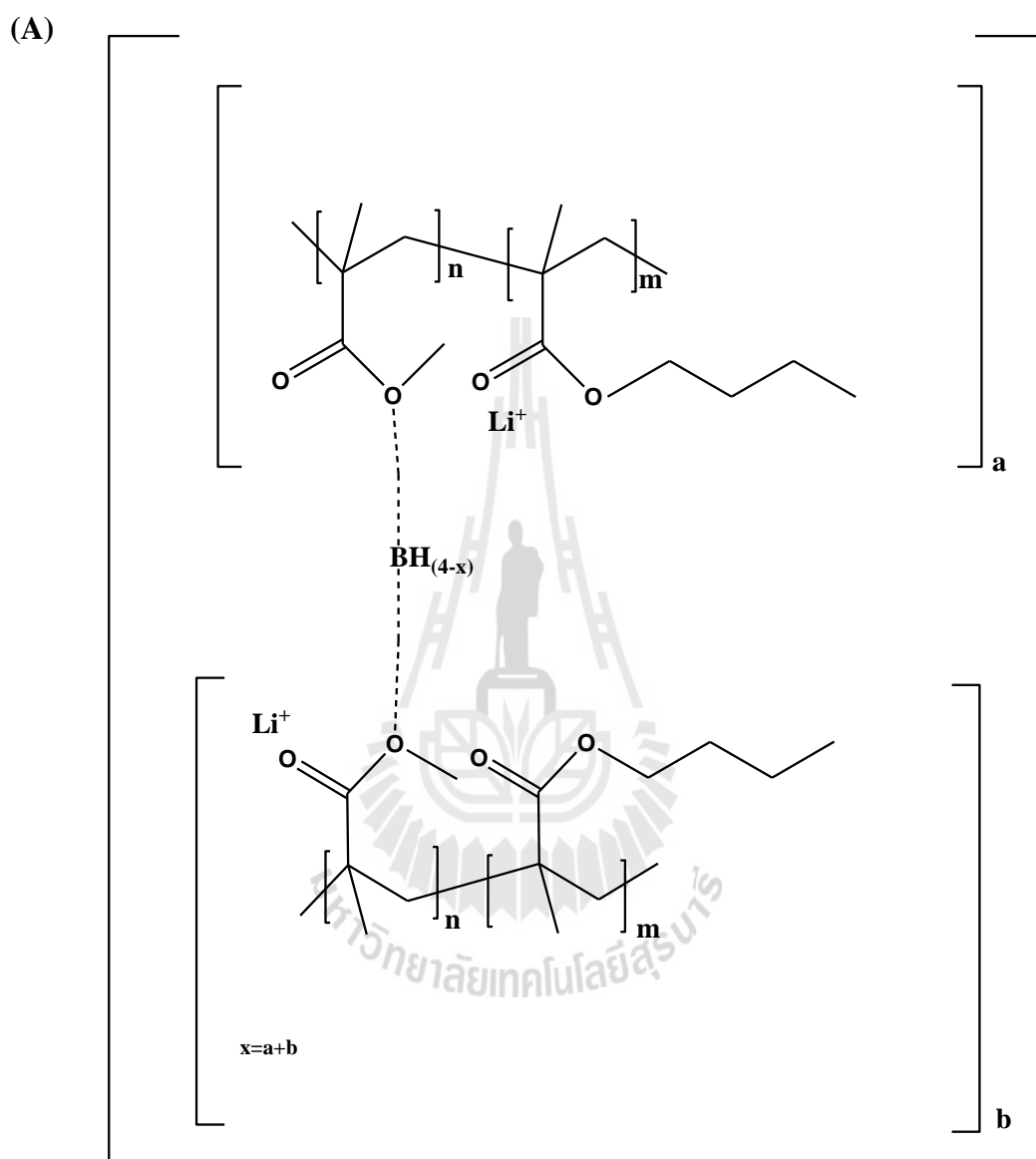


**Figure 4.10** Interaction between PMMA-co-BM and  $\text{LiBH}_4$  at borohydride ( $\text{H}_{(4-x)}\text{B}^{--}(\text{OCH}_3)_x$ ), where  $(a+b)=x$  (A), and boron atoms ( $\text{B}^{--}(\text{OCH}_3)_4$ ) (B).

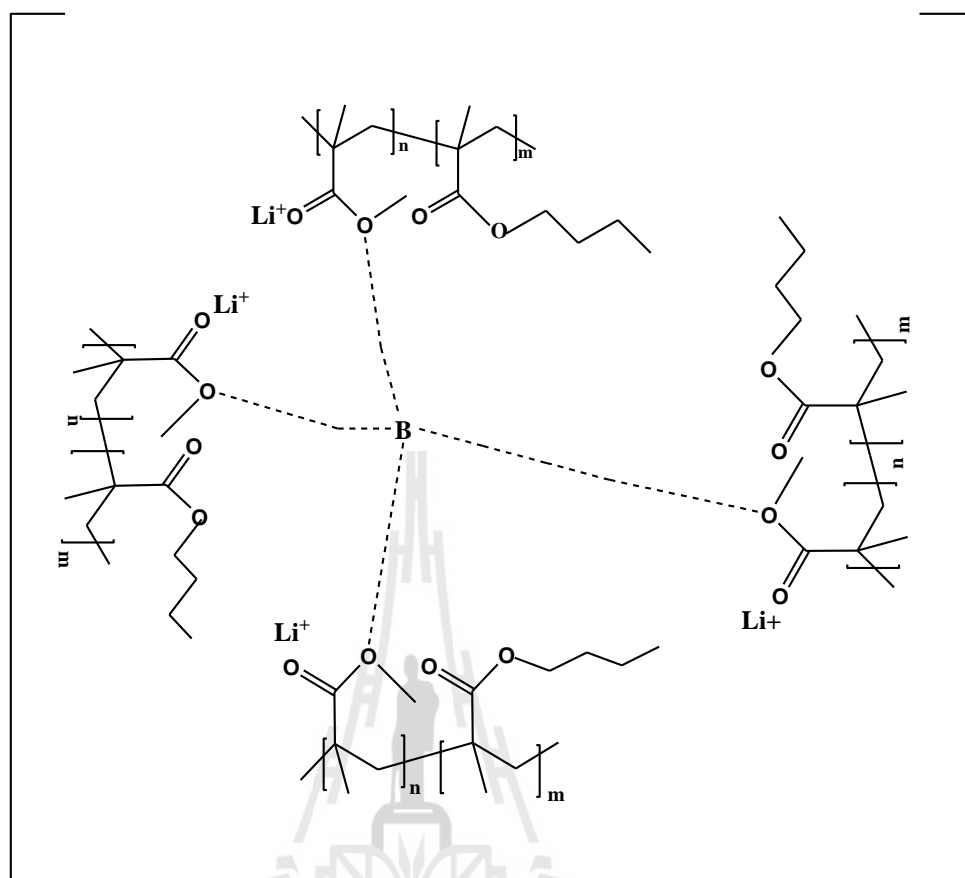


**Figure 4.10** (Continued) Interaction between PMMA-co-BM and  $\text{LiBH}_4$  at borohydride ( $\text{H}_{(4-x)}\text{B}---(\text{OCH}_3)_x$ ), where  $(a+b)=x$  (A), and boron atoms ( $(\text{B}---(\text{OCH}_3)_4)$  (B).

#### 4.1.5 Protection from oxidation and humidity

Use of a PMMA-co-BM polymer matrix for  $\text{LiBH}_4$  nanoconfinement is not only to decrease temperature and pressure for de/rehydrogenation and kinetic improvement, but also to serve as an oxidation and humidity protector for  $\text{LiBH}_4$ , resulting in a practical use in ambient condition. Regarding the hydrophobic surface and higher free volume in the polymer matrix for  $\text{H}_2$  permeability of PMMA-co-BM, contamination of  $\text{LiBH}_4$  nanoconfined in PMMA-co-BM by oxygen and humidity is



diminished. X-ray photoelectron spectroscopy (XPS) was used to investigate the elemental compositions as well as the local chemical environment of the target elements on the sample surface (up to 10 nm depth).

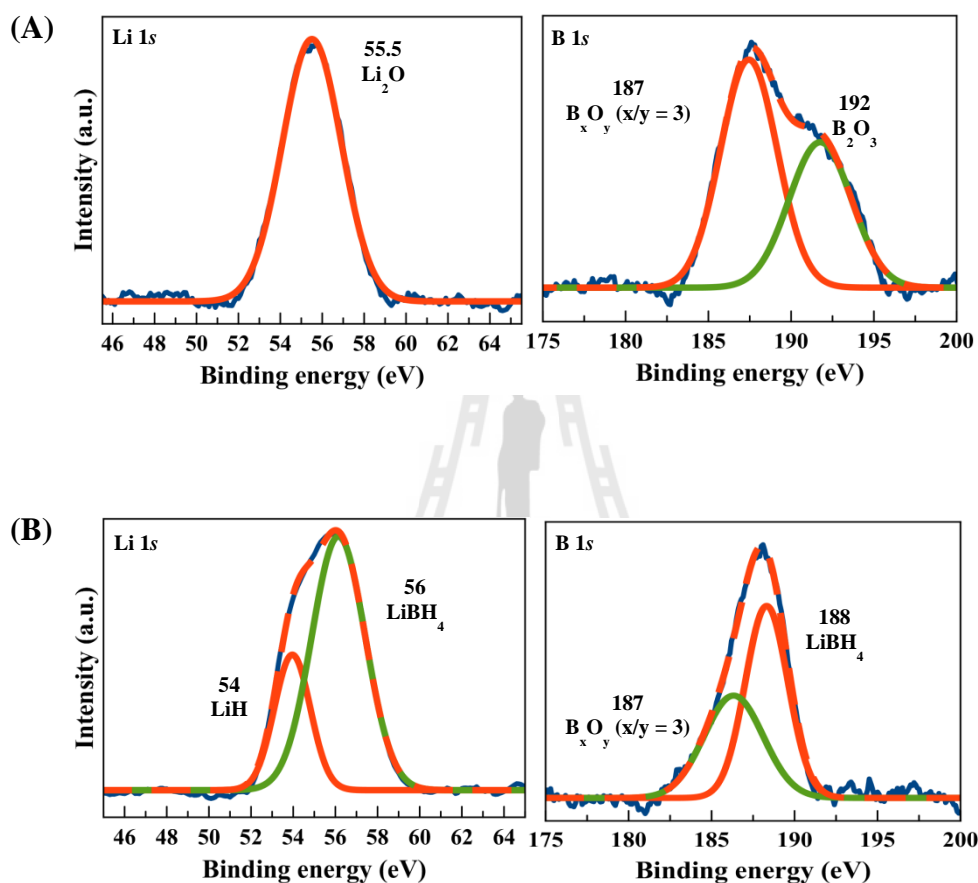


**Figure 4.11**  $\text{Li } 1s$  and  $\text{B } 1s$  spectra of milled  $\text{LiBH}_4$  (A) and nanoconfined  $\text{LiBH}_4$ -PMMA-co-BM before desorption (B).

From Figure 4.11 (A),  $\text{Li } 1s$  of milled  $\text{LiBH}_4$  shows peak of  $\text{Li}_2\text{O}$  at 55.5 eV (Deprez et al., 2011). In the case of  $\text{B } 1s$ , formations of  $\text{B}_2\text{O}_3$  and  $\text{B}_x\text{O}_y$  ( $x/y = 3$ ) are investigated at 192 and 187 eV, respectively (Alexander, www, 2000; Deprez et al. 2011) (Figure 4.11 (A)). The formations of  $\text{Li}_2\text{O}$  and  $\text{B}_2\text{O}_3$  corresponding to oxidation

of  $\text{LiBH}_4$  with oxygen or humidity in air. Moreover, the signal of  $\text{LiBH}_4$  in Li 1s and B 1s are not detected, hinting at instability of  $\text{LiBH}_4$  under ambient condition (25 °C under atmospheric pressure). For nanoconfined  $\text{LiBH}_4$ -PMMA-co-BM, before the XPS experiments the sample was left in ambient environment (25 °C under atmospheric pressure) for 3 days. B 1s spectrum of nanoconfined  $\text{LiBH}_4$ -PMMA-co-BM reveals characteristic peaks of  $\text{LiBH}_4$  at 188 eV together with 187 eV of  $\text{B}_x\text{O}_y$  ( $x/y = 3$ ) (Haipinga et al., 2011; Deprez et al., 2011) (Figure 4.11 (B)). The signal of  $\text{LiBH}_4$  in nanoconfined  $\text{LiBH}_4$ -PMMA-co-BM confirms the ability of PMMA-co-BM polymer matrix to prevent deterioration of  $\text{LiBH}_4$  by oxidation with oxygen and humidity. With respect to 187 eV of  $\text{B}_x\text{O}_y$  ( $x/y = 3$ ) in B 1s spectrum, it should be referred to the interactions between B atoms (and  $\text{BH}_4^-$ ) of  $\text{LiBH}_4$  with methoxyl groups of PMMA-co-BM (i.e.,  $(\text{H}_{(4-x)}\text{B}---(\text{OCH}_3)_x)$  and  $(\text{B}---(\text{OCH}_3)_4)$ , respectively), in accordance with the discussion in section 4.14. In the case of Li 1s, it shows characteristic peaks of  $\text{LiBH}_4$  and LiH at 56.2 and 54.5 eV, respectively (Figure 4.11 (B)) (Haipinga et al., 2011; Fang, et al., 2011). For LiH formation, this suggests partial dehydrogenation of  $\text{LiBH}_4$  during nanoconfinement, in agreement with formation of  $(\text{B}---(\text{OCH}_3)_4)$  and  $(\text{H}_{(4-x)}\text{B}---(\text{OCH}_3)_x)$ . Moreover, the signals of  $\text{LiBH}_4$  found in Li 1s and B 1s spectra of nanoconfined  $\text{LiBH}_4$ -PMMA-co-BM confirmed the oxidation and humidity protection of  $\text{LiBH}_4$  by PMMA-co-BM polymer matrix.

#### 4.1.6 Reaction mechanisms and reversibility

Furthermore,  $^{11}\text{B}$  NMR technique was performed to confirm the reversibility as well as interaction between  $\text{LiBH}_4$  and PMMA-co-BM polymer

matrix. The  $^{11}\text{B}$  NMR spectra in Figure 4.12 (a) presents  $\text{BH}_4^-$  of  $\text{LiBH}_4$  at -37.11 ppm for nanoconfined  $\text{LiBH}_4\text{-PMMA-co-BM}$  together with  $(\text{H}_{(4-x)}\text{B---}(\text{OCH}_3)_x)$  and  $(\text{B---}(\text{OCH}_3)_4)$  at 6.67 and 4.74 ppm, respectively (SDSU Chemistry & Biochemistry Graduate Admissions, www, 2013). At -37.11 ppm, it belongs to  $\text{BH}_4^-$  of  $\text{LiBH}_4$  impregnated in  $\text{PMMA-co-BM}$  polymer matrix (Lee et al., 2012). Moreover, it should be noted that the intensities of  $(\text{B---}(\text{OCH}_3)_4)$ , and  $(\text{H}_{(4-x)}\text{B---}(\text{OCH}_3)_x)$  peaks are almost equivalent, suggesting the comparable fraction of both interactions in nanoconfined  $\text{LiBH}_4\text{-PMMA-co-BM}$ . After complete dehydrogenation at 120 °C under vacuum (Figure 4.12 (b)), signal of  $\text{LiBH}_4$  (-37.11 ppm) disappear as well as the increment of  $(\text{B---}(\text{OCH}_3)_4)$  formation (Figure 4.12 (b)), leading to complete and partial dehydrogenation of  $\text{LiBH}_4$  and  $(\text{H}_{(4-x)}\text{B---}(\text{OCH}_3)_x)$ , respectively.

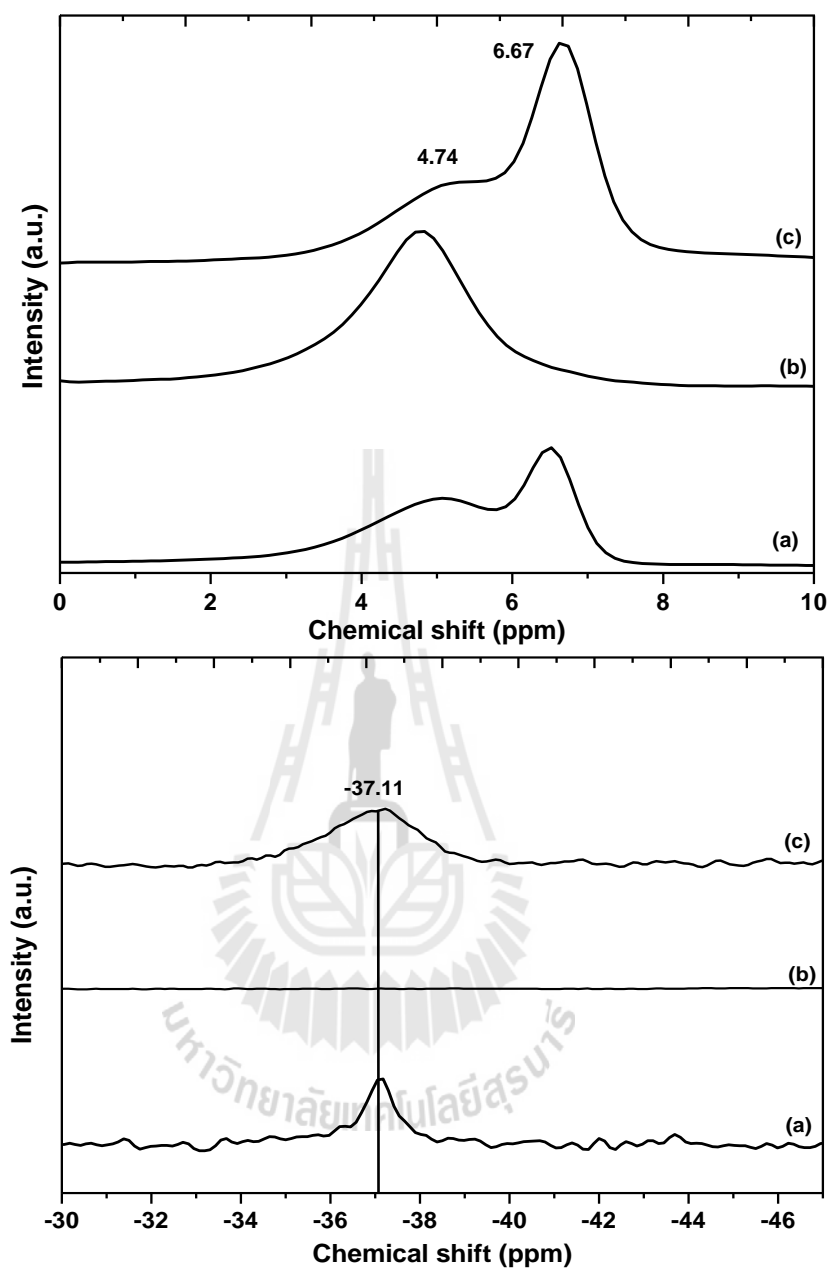


**Figure 4.12**  $^{11}\text{B}$  NMR of nanoconfined  $\text{LiBH}_4\text{-PMMA-co-BM}$  before desorption (a), after desorption (b), and after absorption (c).

With respect to the increase of  $(\text{B}---(\text{OCH}_3)_4)$  formation after dehydrogenation (Figure 4.12 (b)), it could be referred to exothermic peak detected by coupled manometric-calorimetric during dehydrogenation (Figure 4.4). For rehydrogenation

(at 140 °C under 50 bar H<sub>2</sub> for 12 h), it presents BH<sub>4</sub><sup>-</sup> of LiBH<sub>4</sub> and recovered of (H<sub>(4-x)</sub>B---(OCH<sub>3</sub>)<sub>x</sub>) (Figure 4.12 (c)). Therefore, it can be concluded that the nanoconfined LiBH<sub>4</sub>–PMMA–co–BM is completely reversible via reaction of both LiBH<sub>4</sub> and (H<sub>(4-x)</sub>B---(OCH<sub>3</sub>)<sub>x</sub>) formations. Moreover, it is reported that nanoconfinement of LiBH<sub>4</sub> in PMMA–co–BM polymer matrix can help absorbing hydrogen at milder conditions as compared with pure LiBH<sub>4</sub> (T=600 °C under 350 bar H<sub>2</sub>) (Züttel et al., 2003) and nanoconfined LiBH<sub>4</sub> in carbon aerogel (T=400 °C under 100 bar H<sub>2</sub>) (Gross et al., 2008). However, a reduction of hydrogen capacity was obtained from partial dehydrogenation during nanoconfinement due to B---(OCH<sub>3</sub>)<sub>4</sub> formation. Therefore, although the significant destabilization based on the decrease of temperature and pressure for de/rehydrogenation is obtained from nanoconfinement of LiBH<sub>4</sub> in PMMA–co–BM polymer matrix, the interactions between LiBH<sub>4</sub> and PMMA–co–BM (at methoxyl (–OCH<sub>3</sub>) group) and partial thermal degradation of PMMA–co–BM polymer matrix should be reduced for considerable improvement of this hydrogen storage system.

## 4.2 References

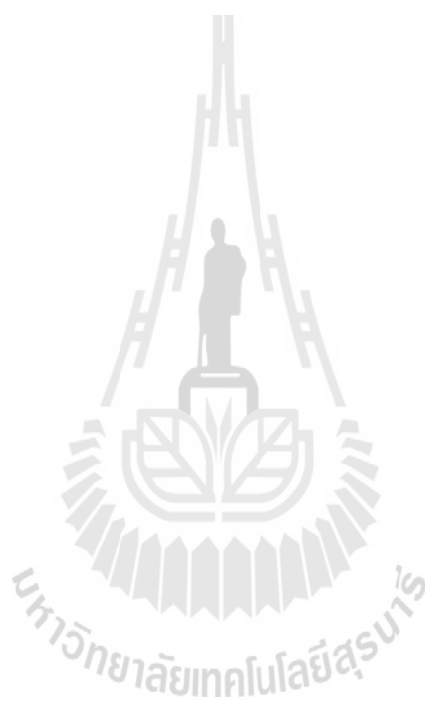
- Alexander, V. (2000). **NIST X-ray Photoelectron Spectroscopy Database** [Online]. Available: <http://srdata.nist.gov/xps/selectEnergyType.aspx>.
- Blanchard, D., Shi, Q., Boothroyd, C. B., and Vegge, T. (2009). Reversibility of Al/Ti Modified LiBH<sub>4</sub>. **J. Phys. Chem. C.** 113: 14059-14066.
- Chang, Z., and LaVerne, J. A. (2001). The gases produced in gamma and heavy-ion radiolysis of poly(methyl methacrylate). **Radiat. Phys. Chem.** 62: 19-24.
- Deprez, E., Munoz-Marquez, M. A., Jimenez de Haro, M. C., Palomares, F. J., Soria,

- F., Dornheim, M., Bormann, R., and Fernandez, A. (2011). Combined x-ray photoelectron spectroscopy and scanning electron microscope studied of the  $\text{LiBH}_4\text{-MgH}_2$  reactive hydride composite with and without a Ti-based additive. **J. Appl. Phys.** 109: 014913-10.
- Fang, Z. Z., Kang, X. D., Yang, Z. X., Walker, G. S., and Wang, P. (2011). Combined effects of functional cation and anion on the reversible dehydrogenation of  $\text{LiBH}_4$ . **J. Phys. Chem. C.** 115: 11839-11845.
- Gross, A. F., Vajo, J. J., Atta, S. L. V., and Olson, G. L. (2008). Enhanced hydrogen storage kinetics of  $\text{LiBH}_4$  in nanoporous carbon scaffolds. **J. Phys. Chem. C.** 112: 5651-5657.
- Haipinga, W., Tiechengb, L., Xuemina, W., Fangfanga, G., Linhonga, C., Honglianga, Z., Chunhonga, L., Xiaohanc, Y., Xind, J., and Weidonga, W. (2011). Corrosion characteristics of  $\text{LiBH}_4$  film exposed to a  $\text{CO}_2/\text{H}_2\text{O}/\text{O}_2/\text{N}_2$  mixture. **Corros. Sci.** 53: 1115-1119.
- Jeon, K. J., Moon, H. R., Ruminski, A. M., Jiang, B., Kisielowski, C., Bardhan, R., and Urban, J. J. (2011). Air-stable magnesium nanocomposites provide rapid and high-capacity hydrogen storage without using heavy-metal catalysts. **Nat. Mater.** 10: 286-290.
- Kashiwagi, T., and Inabi, A. (1989). Behavior of primary radicals during thermal degradation of poly(methyl methacrylate). **Polym. Degrad. Stabil.** 26: 161-184.
- Lee, H. S., Hwang, S. J., Kim, H. K., Lee, Y. S., Park, J., Yu, J. S., and Cho, Y. W. (2012). In situ NMR study on the interaction between  $\text{LiBH}_4\text{-Ca}(\text{BH}_4)_2$  and mesoporous scaffolds. **J. Phys. Chem. Lett.** 3: 2922-2927.

- Li, C., Peng, P., Zhou, D. W., and Wan, L. (2011). Research progress in  $\text{LiBH}_4$  for hydrogen storage: A review. **Int. J. Hydrogen Energ.** 36: 14512-14526.
- Lim, J. S., Noda, I., and Im, S. S. (2008). Effects of metal ion-carbonyl interaction on miscibility and crystallization kinetic of poly(3-hydroxybutyrate-co-3-hydroxyhexanoate)/lightly ionized PBS. **Eur. Polym. J.** 44: 1428-1440.
- Mohlala, P. J., and Strydom, C. A. (2009). FTIR and XPS study of the adsorption of probe molecule used to model alkyd resin adhesion to low carbon aluminium killed steel. **Int. J. Adhes. Adhes.** 29: 240-247.
- Motaung, T. E., Luyt, A. S., Bondioli, F., Messori, M., Saladino, M. L., Spinella, A., Nasillo, G., and Caponetti, E. (2012). PMMA-titania nanocomposites: Properties and thermal degradation behavior. **Polym. Degrad. Stabil.** 97: 1325-1333.
- Namouchi, F., Smaoui, H., Fourati, N., Zerrouki, C., Guermazi, H., and Bonnet, J. J. (2009). Investigation on electrical properties of thermally aged PMMA by combined use of FTIR and impedance spectroscopies. **J. Alloys. Compd.** 469: 197-202.
- Rajkumar, T., Vijayakumar, C. T., Sivasamy, P., Sreedhar, B., and Wilkie, C. A. (2010). Thermal degradation studies on PMMA–HET acid based oligoesters blends. **J. Therm. Anal. Calorim.** 100: 651-660.
- SDSU Chemistry & Biochemistry Graduate Admissions. (2013).  **$^{11}\text{B}$  NMR Chemical Shifts** [On-line]. Available: <http://www.chemistry.sdsu.edu/research/BNMR/>.
- Züttel, A., Wenger, P., Sudan, P., Mauron, Ph. and Emmenegger, Ch. (2003).  $\text{LiBH}_4$  a new hydrogen storage material. **J. Power. Sources.** 118: 1-7.









## CHAPTER V

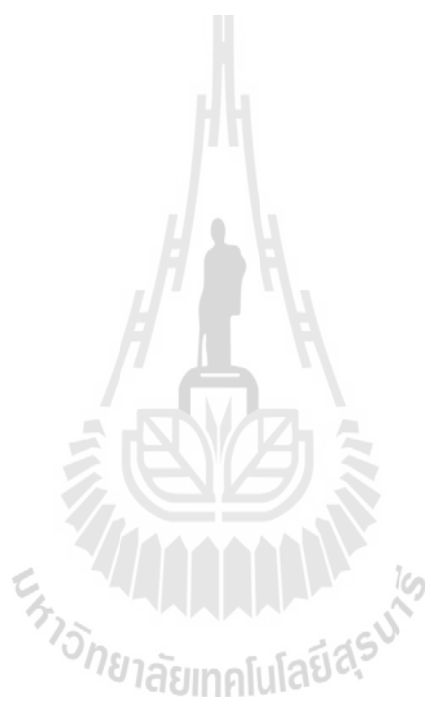
### CONCLUSION

In this thesis, nanoconfined  $\text{LiBH}_4$ -PMMA-co-BM was successfully shown to provide reversible hydrogen storage. Milder de/rehydrogenation conditions and handling in ambient conditions of  $\text{LiBH}_4$  were obtained after nanoconfinement in PMMA-co-BM polymer matrix. The destabilization of  $\text{LiBH}_4$  resulted in the reduction of onset desorption temperature to  $80\text{ }^\circ\text{C}$  ( $\Delta T = 210$  and  $170\text{ }^\circ\text{C}$  as compare with milled  $\text{LiBH}_4$  and nanoconfined  $\text{LiBH}_4$  in carbon aerogel, respectively). Moreover, partial thermal degradation of PMMA-co-BM during dehydrogenation was observed. However, the main gas released from sample during the reaction was hydrogen. Furthermore, rehydrogenation of nanoconfined  $\text{LiBH}_4$ -PMMA-co-BM was obtained under mild conditions ( $140\text{ }^\circ\text{C}$  under 50 bar  $\text{H}_2$  for 12 h). However, with respect to the second hydrogen desorption capacity, it should be due to the partial thermal degradation during the first desorption/absorption, which led to unstable nanoconfinement of  $\text{LiBH}_4$  in PMMA-co-BM polymer matrix. Therefore, the temperature, pressure, and time for rehydrogenation may not be enough to absorb hydrogen completely. With respect to the reaction mechanisms, interaction between  $\text{LiBH}_4$  (boron atoms in the forms of B and  $\text{BH}_4^-$ ) and PMMA-co-BM ( $-\text{OCH}_3$ ) was investigated. Results were not only partial dehydrogenation during sample preparation, but also losses of H and B atoms for  $\text{BH}_4^-$  formation, referring to reduction of hydrogen storage capacity. Although the reduction of de/rehydrogenation

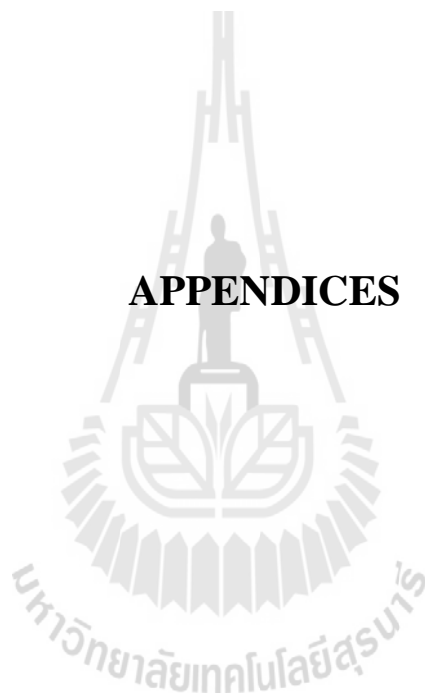
temperature and pressure together with fast kinetics were obtained from nanoconfined  $\text{LiBH}_4$ -PMMA-co-BM, the partial thermal degradation of the PMMA-co-BM as well as interaction between  $\text{LiBH}_4$  and PMMA-co-BM (at methoxyl ( $-\text{OCH}_3$ ) group) should be reduced for improvement of the hydrogen storage system.







# APPENDICES



## APPENDIX A

### CALCULATION OF HYDROGEN CAPACITY

#### A.1 Calculation of theoretical hydrogen storage capacity

- From amount of PMMA-co-BM (5.0656 g) and LiBH<sub>4</sub> (0.66 g), wt. % of LiBH<sub>4</sub> in PMMA-co-BM is calculated by:

$$\begin{aligned}\text{Wt. \% of LiBH}_4 &= (0.66 \text{ g} / (5.0656 \text{ g} + 0.66 \text{ g})) \times 100 \\ &= 11.53 \text{ wt. \%}\end{aligned}$$

- From 13.8 wt. % of hydrogen released by pure LiBH<sub>4</sub>, the theoretical of hydrogen capacity of nanoconfined LiBH<sub>4</sub>-PMMA-co-BM is calculated by:

$$\begin{aligned}\text{Wt. \% of hydrogen} &= (13.8 \text{ wt. \%} \times 11.53 \text{ wt. \%}) / 100 \\ &= 1.59 \text{ wt. \% H}_2\end{aligned}$$

#### A.2 Calculation of hydrogen desorption capacity

- For 1<sup>st</sup> dehydrogenation

$$T = 120 \text{ }^\circ\text{C}$$

$$P_1 = -1.33 \text{ atm}$$

$$P_2 = -0.60 \text{ atm}$$

$$V = 0.024 \text{ L}$$

$$R = 0.0821 \text{ L atm K}^{-1} \text{ mol}^{-1}$$



$$(\Delta P)V = nRT$$

$$\begin{aligned} n &= [(-0.60 \text{ atm}) - (-1.33 \text{ atm})] \times 0.024 \text{ L} / [(0.0821 \text{ L atm K}^{-1} \text{ mol}^{-1}) \times 393 \text{ K}] \\ &= 5.43 \times 10^{-4} \text{ mol} \end{aligned}$$

$$\begin{aligned} \text{H}_2 \text{ desorbed (wt. \%)} &= [(n \times 2.0158) / \text{sample weight}] \times 100 \\ &= [(5.43 \times 10^{-4} \text{ mol} \times 2.0158 \text{ g/mol}) / 0.1402 \text{ g}] \times 100 \\ &= 0.78 \text{ wt. \% H}_2 \end{aligned}$$

➤ For 2<sup>nd</sup> dehydrogenation

$$P_1 = -1.33 \text{ atm}$$

$$P_2 = -1.04 \text{ atm}$$

$$\begin{aligned} n &= [(-1.04 \text{ atm}) - (-1.33 \text{ atm})] \times 0.024 \text{ L} / [(0.0821 \text{ L atm K}^{-1} \text{ mol}^{-1}) \times 393 \text{ K}] \\ &= 2.16 \times 10^{-4} \text{ mol} \end{aligned}$$

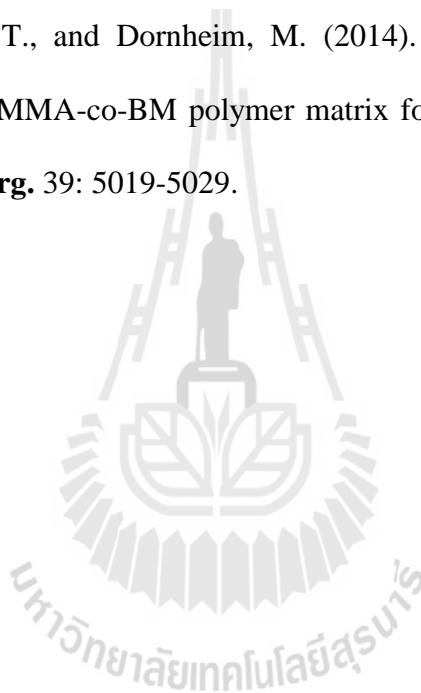
$$\begin{aligned} \text{H}_2 \text{ desorbed (wt. \%)} &= [(2.16 \times 10^{-4} \text{ mol} \times 2.0158 \text{ g/mol}) / 0.1402 \text{ g}] \times 100 \\ &= 0.31 \text{ wt. \% H}_2 \end{aligned}$$

มหาวิทยาลัยเทคโนโลยีสุรนารี

## **APPENDIX B**

### **THESIS OUTPUT**

Gosalawit–Utke. R., Meethom, S., Pistidda, C., Milanese, C., Laipple, D., Saisopa, T., Marini, A., Klassen, T., and Dornheim, M. (2014). Destabilization of  $\text{LiBH}_4$  by nanoconfinement in PMMA-co-BM polymer matrix for reversible hydrogen storage. **Int. J. Hydrogen Energ.** 39: 5019-5029.



## APPENDIX C

ชื่อ

C.1



## CURRICULUM VITAE

**Name** Miss Sukanya Meethom  
**Date of Birth** 26 December 1987  
**Address** 11 Moo 2 Huaitheang District Nakhon Ratchasima Province  
30240, Thailand

### Education

2006-2009 B.Sc. (Chemistry), Rajamankala University of Technology  
Isan, Thailand  
2010-present Student in M.Sc. Program in Biochemistry, Suranaree  
University of Technology, Thailand

### Publications

Gosalawit–Utke, R., Meethom, S., Pistidda, C., Milanese, C., Laipple, D., Saisopa, T.,  
Marini, A., Klassen, T., and Dornheim, M. (2014). Destabilization of  $\text{LiBH}_4$  by  
nanoconfinement in PMMA-co-BM polymer matrix for reversible hydrogen storage.

**Int. J. Hydrogen Energ.** 39: 5019-5029.